ISSN: •2708-6437(Online)
•2708-6429(Print)

Journal of Engineering Advancements

Editor-in-Chief:
Prof. Dr. Mohammad Mashud

Volume 04 Issue 01

SciEn

Published by:
SciEn Publishing Group

Journal of Engineering Advancements

Apt. # 6 C-D, House # 191
Road # 12/A, Dhanmondi R/A
Dhaka-1209, Bangladesh
Email: jea@scienpg.com Website: www.scienpg.com/jea/

Editor-in-Chief

Prof. Dr. Mohammad Mashud
The University of Texas at El Paso, USA
Email: mmashud@utep.edu

Executive Editors

Prof. Dr. Md. Arifuzzaman
Khulna University of Engineering & Technology
Khulna-9203, Bangladesh.
Email: arif48@me.kuet.ac.bd

Prof. Dr. Md. Shariful Islam
Khulna University of Engineering & Technology
Khulna-9203, Bangladesh.
Email: msislam@me.kuet.ac.bd

Editors

Dr. Miklas Scholz
University of Salford
Email: m.scholz@salford.ac.uk

Dr. Abul Mukid Mohammad Mukaddes
Shahjalal University of Science and Technology
Email: mukaddes1975@gmail.com

Dr. Mesbahuddin Chowdhury
University of Canterbury
Email: mesbahuddin.chowdhury@canterbury.ac.nz

Dr. Sabuj Mallik
University of Derby
Email: s.mallik@derby.ac.uk

Dr. Sivakumar Kumaresan
University Malaysia Sabah
Email: shiva@ums.edu.my

Dr. Mohd Suffian Bin Misaran
University Malaysia Sabah
Email: suffian@ums.edu.my

Dr. Yasuhiro Okamura
The University of Tokushima
Email: okamura.yasuhiro@tokushima-u.ac.jp

Dr. Seock Sam Kim
University Malaysia Sabah
Email: sskim@ums.edu.my

Dr. Chu Chi Ming
University Malaysia Sabah
Email: chrischu@ums.edu.my

Dr. Mohammad H. Rahman
University of Wisconsin-Milwaukee
Email: rahmanmh@uwm.edu

Dr. Monir Hossen
Khulna University of Engineering & Technology
Email: mhossen@ece.kuet.ac.bd

Dr. Md. Mizanur Rahman
World University of Bangladesh
Email: mizanur.rahman@mte.wub.edu.bd

Published in: March 2023
Published by: SciEn Publishing Group

Price: Each Issue BDT 200.00 (US$ 15) **ISSN:** 2708-6437 (Online) 2708-6429 (Print)

Journal of Engineering Advancements
Apt. # 6 C-D, House # 191
Road # 12/A, Dhanmondi R/A
Dhaka-1209, Bangladesh
Email: jea@scienpg.com Website: www.scienpg.com/jea/

Published in: March 2023
Published by: SciEn Publishing Group

Price: Each Issue BDT 200.00 (US$ 15) **ISSN:** 2708-6437 (Online) 2708-6429 (Print)

Journal of Engineering Advancements

Volume 04, Issue 01 March 2023

CONTENTS

Original Articles

Sl. No.	Paper Title and Authors	Page No.
01.	Empirical Path Loss Modelling for Selected LTE Networks in FUTA Campus, Ondo State, Nigeria *S. O. Oluwatoki, S. A. Busari, J. J. Popoola*	1
02.	Enhancing Geotechnical Properties of Lateritic Clay with Sawdust Ash-Lime Stabilizer *Oluwafemi O Omotayo, Oluwapelumi O Ojuri, Oluwafemi O Olagunju*	8
03.	Determination of Parameters of Linear Quadratic Regulator using Global Best Inertia Weight Modified Particle Swarm Optimization Algorithm *Agbroko Oghenenyoreme Emakpo, Ogunti Erastus Olarewaju*	14
04.	Development and Performance Evaluation of a Fixed Batch-type Pyrolysis Reactor for Bio-oil Production from Plastic Wastes *Taye Stephen Mogaji, Anthony Omoaka, Olagoke Z. Ayodeji*	19
05.	Numerical Analysis on Cavitation-noise and Fluid-structure Interaction of AU-Outline GAWN Series and B-Series Marine Propellers *Md. Iftekharul Alam, Abidur Rahman Adib, Abdullah Al Rifat, Tafsirul Hassan, Md. Mizanur Rahman*	25

Journal of Engineering Advancements

Published by: SciEn Publishing Group

Apt. # 6 C-D, House # 191, Road # 12/A
Dhanmondi, Dhaka-1209, Bangladesh
Email Address: jea@scienpg.com

www.scienpg.com/jea/

This page is left intentionally blank

SciEn
Journal of Engineering Advancements Vol. 04(01) 2023, pp 1-7 https://doi.org/10.38032/jea.2023.01.001

Empirical Path Loss Modelling for Selected LTE Networks in FUTA Campus, Ondo State, Nigeria

S. O. Oluwatoki, J. J. Popoola and S. A. Busari*

Department of Electrical and Electronics Engineering, Federal University of Technology Akure (FUTA), Ondo State, Nigeria

Received: November 06, 2022, Revised: January 15, 2023, Accepted: January 18, 2023, Available Online: January 31, 2023

ABSTRACT

Deployed Long Term Evolution (LTE) networks in Nigeria can barely meet the desired 100 Mbps downlink throughput leading to unsatisfactory quality of experience by mobile users. Typically, mobile network operators (MNOs) rely on network planning tools designed for generalized environments. These tools employ legacy propagation models that may not be suited to the operational environments under consideration. As such, the efficiency of such legacy path loss models suffers when they are used in environments different from those for which they have been designed, and this poses a major challenge to the MNOs. This is because the Nigerian geographical areas and topographical features vary widely from the areas where the legacy models were developed. Several studies in Nigeria and other African countries have shown that the legacy path loss models perform unsatisfactorily when compared with field measurement data. To address this challenge and enable accurate path loss prediction for an urban campus environment, extensive measurements at 2600 MHz were carried out in the main campus of the Federal University of Technology Akure (FUTA), Ondo State, Nigeria. The measurement results were compared with the path loss predictions from the commonly-used legacy propagation models (Free space and 3GPP TR 36.873). The results show that the legacy path loss models under-predict the path loss averagely by 20-40 dB, and up to 88 dB in some cases, for the considered environment. Root mean square error (RMSE) values in the range of 1.895 and 9.159 were also observed along the routes. The measurement results will enable the MNOs to adjust the path losses in order to deliver improved quality of service.

Keywords: LTE, Propagation Models, Path Loss, Root Mean Square Error, Reference Signal Received Power.

1 Introduction

According to Cisco's visual networking index for 2018–2023, there will be 5.3 billion internet users worldwide by 2023, up from 3.9 billion in 2018 [1]. This results in a huge rise in mobile traffic over the course of five years. For Nigeria, the number of mobile data subscribers was 148 million as at April 2022 for a country with approximately 220 million people [2], [3] showing the high and growing demand for data and broadband services in the country. In order to deliver higher throughput and better quality of service (QoS) and quality of experience (QoE) for the users, the major mobile network operators (MNOs) in Nigeria (including Globacom, MTN, AIRTEL, 9MOBILE, SMILE, and NTEL) have deployed fourth-generation (4G) long-term evolution (LTE) networks. However, the intended 100 Mbps downlink speed [4] is frequently not achieved, resulting in user complaints and discontent, which can lead to regulatory action by the Nigerian Communications Commission (NCC) [5].

To address the challenge and deliver improved QoS by the MNOs, accurate characterization of the wireless channel is highly important. The base station (BS) transmits signals, and as these signals travel across the wireless channel to the receiver (RX), attenuations occur that cause the signal intensity and quality to degrade [5]. The signals are degraded due to distance-dependent attenuation as well as reflection, diffraction, and scattering as they collide with objects in their path. Propagation or path loss (PL) modeling is frequently used to describe this phenomenon. But historically, the propagation models have concentrated on forecasting the received signal strength as well as the signal strength variability at a specific distance from the transmitter (TX). These models are helpful in determining the radio coverage area of a transmitter because they provide signal strength predictions for various TX- RX separation distances [6], [7].

In wireless network planning, propagation models are used to, among other things, estimate cell coverage and evaluate the consequences of interference [6]. There are three major classes of propagation models: stochastic, deterministic and empirical. Stochastic models predict path loss using statistical parameterization. They do not consider environmental peculiarities and therefore have limited accuracies in diverse terrains. The deterministic models, on the other hand, employ ray tracing theories that incorporate environmental parameters to their finest granularity. As a result, deterministic models are computationally complex but they give highly accurate predictions. As for empirical models, they are developed based on field measurements. They are, therefore, site-specific and accurate for the specific propagation environment of interest [7]-[11].

To accurately characterize and predict path loss for a University Campus – which is a hotspot for the MNOs, this study employs the empirical, measurement-based path loss modelling approach. Reference Signal Received Power (RSRP) measurements of LTE BSs of selected operators at 2600 MHz are undertaken. Through fine-tuning their operations, the MNOs will be able to deliver improved QoS and QoE because the resulting path loss models better precisely represent the environment under consideration.

The remainder of the paper is structured as follows: The pertinent material is reviewed in Section 2 of the literature text. Section 3 presents the methodology of the study with respect to

*Corresponding Author Email Address: tokisunday@gmail.com

the measurement procedures and the legacy models used for comparative analyses. Result discussion was presented in Section 4 and Section 5 offers conclusion and recommendation for further studies.

2 Related Works

Various path loss models have been put forth over time for various terrains and frequency ranges. However, there is still much research to be done on how these path loss models perform when utilized in wireless terrains other than those for which they were initially designed [6]. Therefore, as shown by numerous studies around the globe, these models have to be adjusted to the measured data of the specific areas under consideration for accurate performance [12].

The predictions of three empirical propagation models were compared to the measured path loss data at 3.5 GHz in Cambridge in [13]. The findings demonstrated that the COST-231 and Stanford University Interim (SUI) models overestimated path loss in the environment under consideration.The ECC-33 model was suggested for usage in urban settings since it provided the best fit to the measurement data. In [14], the Hata path loss model was optimized for precise prediction suitable for a suburban area in Malaysia using the least-square method. Additionally, tests in the open air in a frequency range of 400 MHz to 1800 MHz were made in Cyberjaya, Malaysia. The Hata model demonstrated the best fit when the measurement results were compared to the current models. The Putrajaya region verified the optimized Hata model, which was used to quantify relative error and assess performance effectiveness. The reduction of mean relative errors was successful, as evidenced by the data.

The authors also provided path loss models for LTE-Advanced networks [14], [15]. Several propagation models, were used to calculate the path loss for different contexts (i.e., remote, partly dense, and cities), all for the 2.3 - 3.5 GHz frequency bands. When comparing other models in the terrain under consideration, the results shows that, COST-231 Hata model provides the least PL for all situations. However, this investigation only uses models with the least path loss and did not contrast the forecast of classical models with that of conventional models.

Similarly, extensive measurement campaigns at 3.4 GHz frequency were undertaken in Lagos, Nigeria and presented in [10]. Six classical path loss models were compared with the measurement results. The COST 231-Hata and Ericson models were shown to perform the best in urban and suburban regions. Additionally, the authors of [16] used data gathered in urban Nigerian cities to create the path loss models to assess the effectiveness of empirical, heuristic, and geographical methodologies used for signal path loss predictions. The resulting models were compared to field data that was measured. All models, with the exception of the ECC-33 and Egli models, provided acceptable root mean square error (RMSE) values. The three methods submitted were straightforward to use and were most frequently used.

Additionally, research has been done to compare the path loss of city and suburb areas to determine whether certain propagation model can be applied in the two environments. The authors of [17] demonstrated that compared to suburban areas, metropolitan areas experience larger losses in propagation models. In all settings, it was impossible to recommend just one generic model. Authors [18], examined 4G LTE BS's throughput performance to see whether LTE can support data requirements of broadband applications.

The 4G LTE BS running on 2600 MHz that was deployed in Ghana gave the highest recorded output of 29.9 Mbps in each sector in the field. Users around 2.5 km of the cell range from the BS experienced the highest downlink throughput of 62.318 Mbps. These established that 4G LTE can satisfy Ghanaians' rising demand for broadband. After contrasting these throughputs with desired outputs necessary to support data-centric broadband usage, this result was reached.

Further, the author of [19], examined the path loss of mobile radio series in L-band frequency (i.e., 800 MHz) in Akure, South Western Nigeria. The city of Akure is a dense urban environment. Measurements were carried out to determine the received signal strength (RSS) of MTN network within the Akure metropolis. The analysis did not take into account the 2600 MHz spectrum being considered in this article and instead concentrated on the 800 MHz band. Also, the study was limited to only one MNO (i.e., MTN) and did not consider multiple MNOs as studied in this work.

It is crucial to choose the optimum model for each environment under consideration because different path loss models perform differently in various settings. As far as the authors are aware, no research has examined the path loss for the FUTA campus setting for LTE networks from various MNOs. This study, therefore, addresses this gap and aims to not only enable operators deliver improved QoS but also facilitate seamless connectivity and enhanced QoE and customer satisfaction.

3 Field Measurements

In this section, we present the procedures for the field measurements carried out and describe the considered environment as well as the legacy path models used for comparison.

3.1 Measurement Procedures

For the empirical path loss modelling approach considered in this work, reference signal received power (RSRP) measurement values were taken along three different routes within the main campus of the Federal University of Technology Akure (FUTA), Ondo State, Nigeria. The size of the FUTA campus is 640 hectares ($\mathrm{i.e.}, 6.4\ km^2$) [20]. The drive tests were conducted using smartphones pre-installed with an LTE software app named Cell Tower Locator connector [21]. The smartphone was connected to a computer via the universal serial bus (USB) port. The Cell Tower Locator probe is a software instrument for data collection. Location and distance were determined using the global positioning system (GPS). For six different LTE BSs operating on 2600 MHz carrier frequency on the campus, RSRP values were measured at intervals of 10 m away, and up to 1000 m away from the respective BSs. The starting reference distance (d_r) of 10 m was used.

The height of the mobile antenna receiver of 1.5m was kept constant during the measurements. The personal device, maintaining information gathered, also received the measured data via the phones. After then, post-processing and analysis were performed on these record log files. From February through May 2022, field measurements were made. Both line of sight (LOS) and non-LOS were used to measure the RSRP (dBm) values. The BSs of the different MNOs have varied transmitter heights between 16 m and 40 m. Fig. 1 shows the measurement system setup.

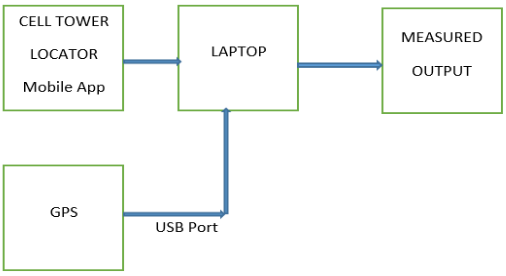

Fig. 1 Measurement setup block diagram.

Table 1 Assignment Table for Ondo State, Nigeria Frequency

2.6 GHz BAND FOR ONDO STATE NIGERIA				
PARAMETERS	**FDD**		**TDD**	
CHANNEL BLOCK	A1	B1	C1	D
MOBILE NETWORK OPERATOR	AIRTEL	MTN	OPEN SKY	MEGATECH
BANDWIDTH	20 MHz	30 MHz	10 MHz	40 MHz
TX Frequency (MHz)	2500-2520	2520-2550	2560-2570	2575-2615
RX Frequency (MHz)	2620-2640	2640-2670	2680-2690	

3.2 Environmental Details

Several test measurements were collected along the stated three routes (A, B and C) of the FUTA main campus as shown in the map of Fig. 2 and as described thus:

Route A: This route is from the Center for Renewable Technology (CRET) to the Middle Belt area (close to the School of Engineering and Engineering Technology (SEET), Obanla, Ondo State, South West Region of Nigeria). The coordinates for CRET are: 7° 18' 11.322" N (latitude), 5° 7' 38.1288" E (longitude) while the coordinates for Middle Belt are: 7° 18' 13.032" N (latitude), 5° 8' 13.668" E (longitude). The route is a flat terrain with a few high rise buildings separated apart with vegetation.

Route B: This route is from the School of Environmental Technology (SET) to the Middle Belt, FUTA. The coordinates for SET are: 7° 17' 56.3244" N (latitude), 5° 8' 14.0748" E (longitude) while the coordinates for Middle Belt are: 7° 18' 13.032" N (latitude), 5° 8' 13.668" E (longitude). The route is characterized with high rise buildings, automobiles and machines.

Route C: This route is from the Students' Union Building (SUB) to the Middle Belt area of the University campus. The coordinates for SUB are: 7° 18' 15.264" N (latitude), 5° 8' 46.0644" E (longitude) while the coordinates for Middle Belt are: 7° 18' 13.032" N (latitude), 5° 8' 13.668" E (longitude). The route is characterized as an urban area due high rising buildings, few vegetation, automobiles and business areas.

Base Stations Locations: CRET (MTN / AIRTEL), SET (MTN / AIRTEL) and SUB (MTN / AIRTEL).

3.3 Network Parameters

The parameters used to create the path loss models for various routes are listed in Table 2. For all locations and networks, the carrier frequency is 2600 MHz, distance covered in each route is 10 -1000 m, reference distance (d_r) is 10 m while the receiver antenna height is 1.5 m throughout the measurement campaign.

Table 2 Network Parameters

S/N	Location	MNO BS	TX. antenna height (m)	TX. Power (dB)
1.	CRET	MTN	40	13.5
		AIRTEL	32	18.0
2.	SET	MTN	30	12.5
		AIRTEL	32	18.0
3.	SUB	MTN	32	3.1
		AIRTEL	32	18.0

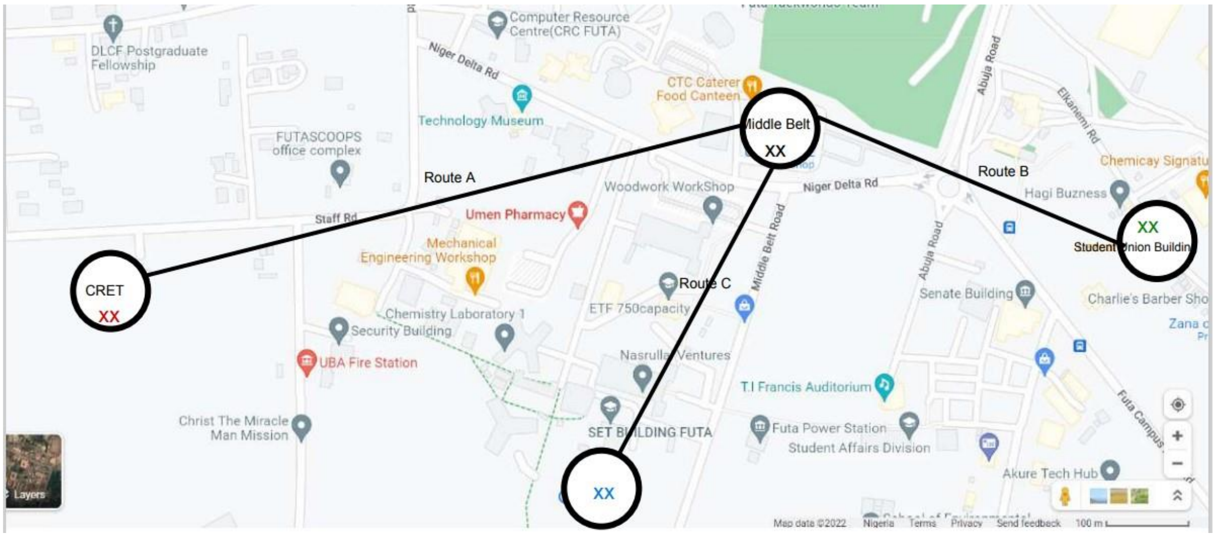

Fig. 2: Map of all considered routes of the FUTA Campus (Akure, Ondo State, Nigeria).

3.4 Propagation Models

The measurement-based path loss model developed in this study is compared to the following legacy path loss models.

3.4.1 Free Space Path Loss

The free space path loss (FSPL) model [22] is given in Eq. (1)

$$PL = 32.45 + 20\,log_{10}(d) + 20\,log_{10}(f) \qquad (1)$$

The frequency is denoted as f (MHz) and distance is d (km).

3.4.2 3GPP TR 36.873 (3D Urban-Macro) Channel Model

The Third Generation Partnership Project (3GPP) TR 36.873's three dimensional (3D) channel model is used for comparison because it is applicable for the frequency range 0.5-6 GHz [23]. Using the model, the path losses for LOS and NLOS are given by Eq. (2) and Eq. (3), respectively:

$$PL_{los} = \begin{cases} 28 + 22\,log_{10}(d_{3D}) + 20\,log_{10}(f). & 10 < d_{2D} < d_{BP} \\ 28 + 40\,log_{10}(d_{3D}) + 20\,log_{10}(f) - 9\,log_{10}\left((d_{BP})^2 + ((25 - h_{UE})^2)\right). & d_{BP} < d_{2D} < 500 \end{cases} \qquad (2)$$

$$PL_{Nlos} = 69.51 + 39.09\,log_{10}(d_{3D}) + 20\,log_{10}(f) + 7.5\,log_{10}(h_{UE}) - 0.6h_{UE} - 0.0825(h_{UE})^2 \qquad (3)$$

where the shadow fading (SF) for LOS is 4 dB and SF for NLOS is 6 dB; f (GHz) is frequency, $d_{2D}(m)$ is the two dimensional (2D) separation distance, $d_{3D}(m)$ is the 3D distance and $h_{UE}(m)$ *denote the* height of the user equipment (UE) or the mobile receiver.

The breakpoint distance d_{BP} is given $d_{BP} = 320\big((h_{UE} - 1)fc\big)$ [24] for the urban-macro (UMa) setting considered in this work. The LOS probability Pr_{LOS} is evaluated using Eq. (4)-(6).

$$Pr_{LOS} = \left(min\left(\frac{18}{d_{2D}}, 1\right)\left(1 - exp\left(\frac{-d_{2D}}{63}\right)\right) + exp\left(\frac{-d_{2D}}{63}\right)\right)\big(1 + C(d_{2D}, h_{UE})\big) \qquad (4)$$

$$C(d_{2D}, h_{UE}) = \begin{cases} 1, & d_{2D} \le 18 \\ 1 + 1.25C'(h_{UE})\left(\frac{d_{2D}}{100}\right)^3 exp\left(\frac{-d_{2D}}{150}\right), h_{UE} \le 13 & 18 < d_{2D} \end{cases} \qquad (5)$$

$$C'(h_{UE}) = \begin{cases} 0, & \\ \left(\frac{h_{UE} - 13}{10}\right)^{1.5}, & 13 < h_{UE} \le 23 \end{cases} \qquad (6)$$

3.5 Performance Metrics

The following metrics were used to assess and compare the models' performance:

3.5.1 Path Loss Exponent

From the measured data, for each of the routes taken into consideration, the path loss exponent (n) was calculated. It illustrates the lossy nature of the specific propagation terrain. The path loss exponent is computed using Eq. (7) [25]:

$$n = \frac{\sum_{i=1}^{k}\left(Pl_{d_r} - P_i\right) \times 10\,log\left(\frac{d}{d_r}\right)}{\sum_{i=1}^{k}\left(10log\left(\frac{d}{d_r}\right)\right)^2} \qquad (7)$$

where, n denotes the path loss exponent, separation distance is denoted as d, measured data point is k, and p_i denotes the power received at the reference distance (d_r), the path loss at reference distance is denoted as Pl_{d_r}.

3.5.2 Root Mean Square Error

The difference between the signal power predicted by a model and the actual measured signal is quantified by the root mean square error (RMSE). Comparing the prediction errors of the various propagation models with the provided measurement data provides a measure of accuracy. Computed RMSE values were obtained using Eq. (8):

$$RMSE = \sqrt{\frac{\sum_{k=1}^{k}[p_i - \widehat{p_i}]^2}{k}} \qquad (8)$$

where k is the number of measured samples, p_i is the measured power value at a given distance, $\widehat{p_i}$ is the predicted power value at a given distance.

4 Results and Analysis

In this section, measurement results are presented for the selected MNOs (MTN-Nigeria and Airtel-Nigeria) for the 2600 MHz frequency along the three routes of the FUTA campus considered in this study.

4.1 RSRP Results

The RSRP results for MTN and Airtel BSs along the three routes (Routes A, B and C) are shown in Fig. 3. Established average received power for each measurements were achieved by averaging the data taken at each point from the BS antennas. Each result indicates the power received computed against distances of two different LTE networks (MTN-Nigeria and Airtel-Nigeria) deployed within the FUTA campus. The RSRPs are plotted against distances as shown in Fig. 3. The results show decrease in the RSRP measurement values as the receiver moves away from the base stations of each network. The decay is due to the distance-dependent attenuation with increasing distance, and the variations in measured values of the same network along different routes are attributable to the differences in shadow fading (due to obstacles) and terrain of the different routes.

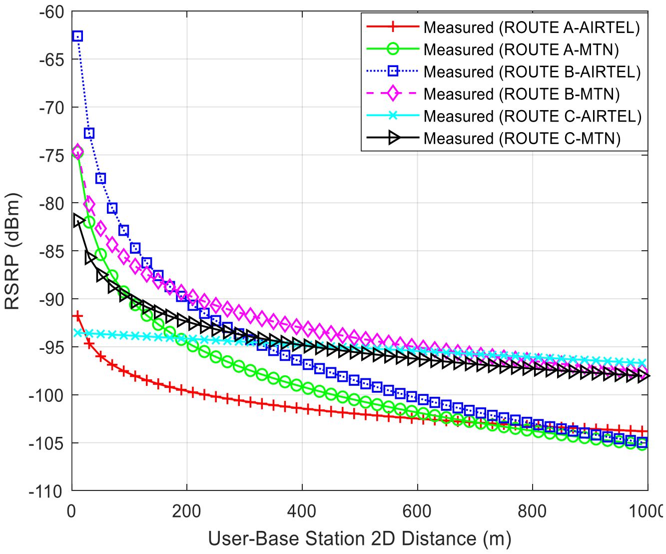

Fig. 3: RSRP of all Routes.

4.2 Path Loss Results

The following formula (Eq. (9)) was employed to determine the path loss at each measured site with distance d (m):

$$PL\ (dB) = E\ (dBm) - P_{mr}\ (dBm) \tag{9}$$

where $P_{mr}\ (dBm)$ is the mean received power, the E (dBm) is the effective isotropic radiated power and $PL\ (dB)$ is the path loss. The E is further given by Eq. (10).

$$E = P_{tx} + G_s - L_s \tag{10}$$

where G_s and L_s stands for gains and losses respectively. Antennas gains at both the transmitter and receiver ends are typically taken into account, and connector, body and combiner losses are typically considered as well Eq. (11).

$$E = P_{tx} + G_{tx} + G_{mrx} - L_c - L_{co} - L_b \tag{11}$$

P_{tx} Stands for transmit power (dBm), G_{tx} for the antenna transmit gain (dBi), G_{mrx} for antenna gain of the mobile receiver antenna (dBi), L_{co} for connector loss (dB), L_b denotes the body loss (dB) and L_c is given as combiner loss (dB). These parameter's actual values for LTE are given in [26] and substituted into (10) for the E. In order to determine the path loss, the estimated values of E (dBm) and $P_{mr}\ (dBm)$ are then substituted into (9). Fig. 4 displays the resulting path loss for all the routes. Plots of path loss against distance were used to examine the impact of increasing distance on PL as illustrated.

It can be seen from Fig. 4 that as distance increases from the BS, the path loss also increases. Comparing the computed path losses along the routes for the same network, the differences in the path loss values obtained along the different routes is due to differences in the BS parameters as given in Table 2, thus justifying Fig. 4.

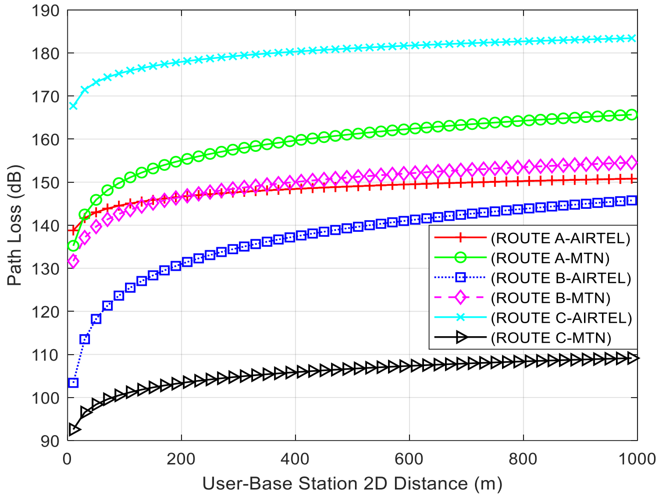

Fig. 4: Measured Path Loss of all Routes.

4.2.1 Path Loss Measurement Results Compared to Legacy Models

Each observed environment's path loss is compared to the two legacy path loss models' estimated path losses (i.e., the FSPL [22] and the 3GPP TR 36.873 (Urban-Macro-3D) [24]) at 2600 MHz for urban area of the FUTA campus, for the two networks (i.e., MTN and Airtel). Fig. 5, Fig. 6 and Fig. 7 Shows the respective results for the three routes plots. The results show that the two classical models under-predict the path losses along the three routes.

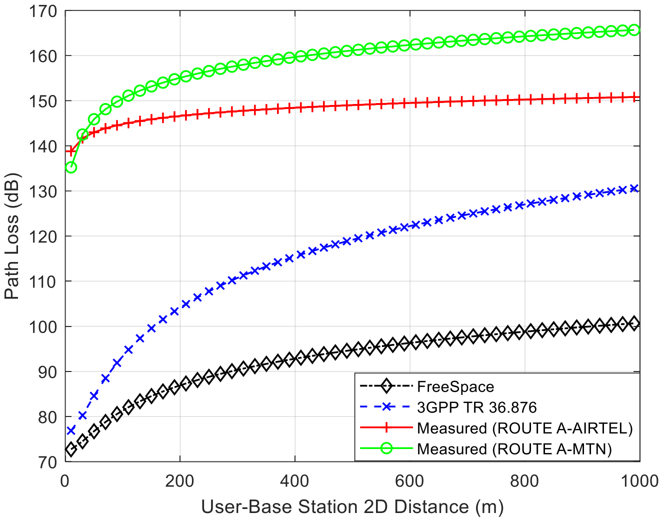

Fig. 5: Route A Path Loss.

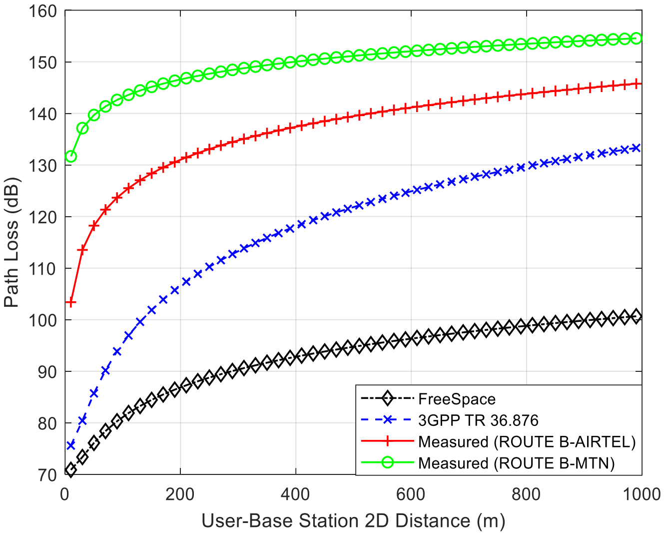

Fig. 6: Route B Path Loss.

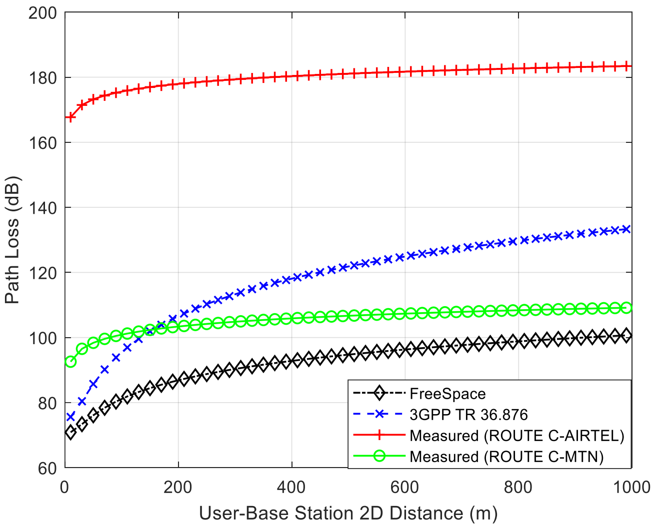

Fig. 7: Route C Path Loss.

4.2.2 Result Analysis

Table 3a and Table 3b show the summary of path losses against distances. Few samples (i.e., at 400 and 800 m) were considered and compared generated path loss measured data against legacy path loss models at stated distance in other to observe and come out with reasonable results of the models along each route.

Table 3a Path Loss Summary Result

	Measured Path Loss against Distance		Legacy Path Loss against Distance	
	MTN	**Airtel**	**3GPP TR 36.873**	**Free Space**
Route A	159.67 dB @ 400 m	148.43 dB @ 400 m	115.49 dB @ 400 m	92.83 dB @ 400 m
	164.26 dB @ 800 m	150.25 dB @ 800 m	127.01 dB @ 800 m	98.82 dB @ 800 m
Route B	150.04 dB @ 400 m	137.40 dB @ 400 m	118.09 dB @ 400 m	92.81 dB @400 m
	153.49 dB @ 800 m	143.79 dB @ 800 m	129.72 dB @ 80 0 m	98.82 dB @ 800 m
Route C	105.88 dB @ 400 m	180.32 dB @ 400 m	118.09 dB @ 400 m	92.81 dB @ 400 m
	108.38 dB @ 800 m	182.69 dB @ 800 m	129.72 dB @ 800 m	98.82 dB @ 800 m

Table 3b shows the summary of the differences between the measured path loss and the legacy path loss model results of the two considered MNOs (MTN and Airtel) on the three routes in the FUTA campus while maintaining the same distance as stated in Table 3a.

Table 3b Differences between Measured and Legacy Path Loss Results

	Measured - Legacy Path Loss		Measured - Legacy Path Loss	
	MTN-3GPP TR 36.873	**MTN- Free Space**	**Airtel - 3GPP TR 36.873**	**Airtel - Free Space**
Route A	44.177 dB @ 400 m	66.833 dB @ 400 m	32.944 dB @ 400 m	55.605 dB @ 400 m
	37.426 dB @ 800 m	65.442 dB@ 800 m	23.239 dB @ 800 m	51.428 dB @ 800 m
Route B	31.941 dB @ 400 m	57.222 dB @ 400 m	19.309 dB @ 400 m	44.59 dB @ 400 m
	23.765 dB @ 800 m	54.673 dB @ 800 m	14.07 dB @ 800 m	44.978 dB @ 800 m
Route C	-12.219 dB @ 400 m	13.061 dB @ 400 m	62.223 dB @ 400 m	87.503 dB @ 400 m
	-21.35 dB @ 800 m	9.56 dB @ 800 m	52 dB @ 800 m	83.872 dB @ 800 m

4.2.2.1 Route A

Considering the path loss for Route A results shown in Fig. 5, Table 3a and Table 3b , we analyze the results of the measured data path loss against distance in comparison with legacy path loss models such as the free space and 3GPP TR 36.873 models.

At 400 m of MTN the differences between the measured path loss and legacy path loss models are 44.177 dB (3GPP TR 36.873) and 66.833 dB (Free Space) while for Airtel network at same distance the differences are 32.944 dB (3GPP TR 36.873) and 55.605 dB (Free Space). At 800 m for MTN network, the difference between the measured path loss and legacy path loss models are 37.426 dB (3GPP TR 36.873) and 65.442 dB (Free Space) while for the Airtel network at same distance, the differences are 23.239 dB (3GPP TR 36.873) and 51.428 dB (Free Space).

4.2.2.2 Route B

Next we consider the path loss analysis for Route B results shown in Fig. 6, Table 3a, and Table 3b. For MTN at 400 m, the differences between the measured path loss and legacy path loss models are 31.941 dB (3GPP TR 36.873), 57.222 dB (Free Space) while for Airtel network at same distance the differences are 19.309 dB (3GPP TR 36.873) and 44.59 dB (Free Space). At 800 m of MTN network the difference between the measured path loss and legacy path loss models are 23.765 dB (3GPP TR 36.873) and 54.673 dB (Free Space) while for Airtel network at same distance, the differences are 14.07 dB (3GPP TR 36.873) and 44.978 dB (Free Space).

4.2.2.3 Route C

For Route C, we consider the path loss analysis for the results shown in Fig. 7, Table 3a, and Table 3b. At 400 m for MTN, the differences between the measured path loss and legacy path loss models are: -12.219 dB (3GPP TR 36.873) and 13.061 dB (Free Space) while for Airtel network at same distance the differences are 62.223 dB (3GPP TR 36.873) and 87.503 dB (Free Space). At 800 m for MTN network, the differences between the measured path loss and legacy path loss models are -21.35 dB (3GPP TR 36.873) and 9.56 dB (Free Space) while for Airtel network at same distance, the differences are 52 dB (3GPP TR 36.873), and 83.872 dB (Free Space).

Overall, the path loss values along the three routes show that the 3GPP TR 36.873 and the FSPL under-predicted the path loss, in some cases by up to approximately 88 dB for the considered environment.

4.3 RMSE Results

The RMSE results for the measurement data as compared to the predictions form legacy path loss models are given in Table 4. The lower the RMSE value, the better suited is the model for the environment under consideration [7].

Table 4 RMSE Values

Route	RMSE
Route A (Airtel)	5.766
Route A (MTN)	7.287
Route B (Airtel)	9.159
Route B (MTN)	5.561
Route C (Airtel)	6.375
Route C (MTN)	1.895

5 Conclusion

This study investigated a measurement-based path loss modelling for a University campus environment, using two LTE networks' measurement data, each network measurement taken around three routes on the campus. The measurement results are compared to the FSPL and the 3GPP TR 36.873 path loss models. Analyses of the results (using path loss and RMSE) show that the legacy models under-predict the path loss for the considered environment. The measurement-based results will enable the MNOs to accurately characterize their network by adjusting their predicted path losses and enable them to deliver improved QoS. This will translate to the improved QoE and customer satisfaction for the users. Future works will consider other carrier frequencies and MNOs.

References

[1] Cisco, V. N. I, “Cisco Annual Internet Report Highlights tool: Forecast and trends, 2018–2023. White Paper, 1,” 2022.

[2] Naira metrics, “Industry data released by the Nigerian Communications Commission (NCC) Nigeria’s internet subscription hits 148 million in April 2022.” 2022.

[3] World Population Review, “World Population Review. (2022). Nigerian Population. Retrieved 18th July 2022 from http: // Nigeria Population 2022 (Demographics, Maps, Graphs),” Nigeria Population 2022 (Demographics, Maps, Graphs), 2022. [Online]. Available: worldpopulationreview.com

[4] National Independent Wireless Broadband Quality, “Enextgen Wireless releases NIWBQR report on quality of 4G LTE networks in Akure,” Aug. 17, 2021. [Online]. Available: https://techeconomy.ng/2021/08/enextgen-wireless-releases-niwbqr-report-on-quality-of-4g-lte-networks-in-akure/

[5] NCC, “NCC complaint management procedures and resolutions. Retrieved 18th July 2022 from NCC FPC NEW.cdr,” complaint management procedures and resolutions. Retrieved, Jul. 2022, [Online]. Available: https://www.ncc.gov.ng/docman-main/industry-statistics/policies-reports/882-cab-consumer-complaint-report-202004/file

[6] Rappaport, T.S., 1996. *Wireless communications: principles and practice* (Vol. 2). New Jersey: prentice hall PTR.

[7] Halifa, A., Tchao, E.T. and Kponyo, J.J., 2017. Investigating the best radio propagation model for 4G-WiMAX networks deployment in 2530MHz Band in Sub-Saharan Africa. *arXiv preprint arXiv:1711.08065*..

[8] Chebil, J., Lawas, A.K. and Islam, M.D., 2013. Comparison between measured and predicted path loss for mobile communication in Malaysia. *World Applied Sciences Journal*, *21*(21), pp.123-128.

[9] Mollel, M. and Michael, K., 2014. Comparison of empirical propagation path loss models for mobile communication. *Computer Engineering and Intelligent Systems*, *5*(9).

[10] Ibhaze, A.E., Imoize, A.L., Ajose, S.O., John, S.N., Ndujiuba, C.U. and Idachaba, F.E., 2017. An empirical propagation model for path loss prediction at 2100MHz in a dense urban environment. *Indian Journal of Science and Technology*, *10*(5), pp.1-9.

[11] Ajose, S.O. and Imoize, A.L., 2013. Propagation measurements and modelling at 1800 MHz in Lagos Nigeria. *International Journal of Wireless and Mobile Computing*, *6*(2), pp.165-174.

[12] Imoize, A.L., Ibhaze, A.E., Nwosu, P.O. and Ajose, S.O., 2019. Determination of Best-Fit Propagation Models for Pathloss Prediction of a 4G LTE Network in Suburban and Urban Areas of Lagos, Nigeria. *West Indian Journal of Engineering*, *41*(2).

[13] Abhayawardhana, V.S., Wassell, I.J., Crosby, D., Sellars, M.P. and Brown, M.G., 2005, May. Comparison of empirical propagation path loss models for fixed wireless access systems. In *2005 IEEE 61st Vehicular Technology Conference* (Vol. 1, pp. 73-77). IEEE.

[14] Roslee, M.B. and Kwan, K.F., 2010. Optimization of Hata propagation prediction model in suburban area in Malaysia. *Progress In Electromagnetics Research C*, *13*, pp.91-106.

[15] Kale, A.J.S.S. and Jadhav, A.N., 2013. An Empirically Based Path Loss Models for LTE Advanced Network and Modeling for 4G Wireless Systems at 2.4 GHz, 2.6 GHz and 3.5 GHz. *International Journal of Application or Innovation in Engineering & Management (IJAIEM)*, *2*(9), pp.252-257.

[16] Faruk, N., Popoola, S.I., Surajudeen-Bakinde, N.T., Oloyede, A.A., Abdulkarim, A., Olawoyin, L.A., Ali, M., Calafate, C.T. and Atayero, A.A., 2019. Path loss predictions in the VHF and UHF bands within urban environments: experimental investigation of empirical, heuristics and geospatial models. *IEEE access*, *7*, pp.77293-77307.

[17] Khan, I., Eng, T.C. and Kamboh, S.A., 2012. Performance analysis of various path loss models for wireless network in different environments. *International Journal of Engineering and Advanced Technology (IJEAT)*, *2*(1), pp.161-65.

[18] Tchao, E.T., Gadze, J.D. and Agyapong, J.O., 2018. Performance evaluation of a deployed 4G LTE network. *arXiv preprint arXiv:1804.05771*.

[19] Ojo, J.S., Adekunle, A. and Falodun, S.E., 2014. Investigation of path loss of mobile radio service at l-band frequency over Akure, South western Nigeria. *IOSR Journal of Electronics and Communication Engineering*, *9*(2), pp.126-132.

[20] Adekunle, V.A.J., 2007. Ecological and environmental implications of national development: A case study of Obanla natural forest, Federal University of Technology, Akure, Nigeria. *Research Journal of Environmental Science*, *4*, pp.127-140.

[21] “Cell Tower Locator App”, [Online]. Available: https://play.google.com/store/apps/details?id=ru.v_a_v.celltowerlocator&hl=en&gl=US

[22] Gibson, D. J., THE COMMUNICATIONS HANDBOOK. USA. CRC Press, Inc, 1996.

[23] Busari, S.A., Huq, K.M.S., Mumtaz, S. and Rodriguez, J., 2018, December. Impact of 3D channel modeling for Ultra-High speed beyond-5G networks. In *2018 IEEE Globecom Workshops (GC Wkshps)* (pp. 1-6). IEEE.

[24] 3rd Generation Partnership Project (3GPP), 2015. Study on 3D channel model for LTE. *3GPP TR 36.873 V12. 2.0, Tech. Rep*.

[25] Zhou, T., Sharif, H., Hempel, M., Mahasukhon, P., Wang, W. and Ma, T., 2009, October. A deterministic approach to evaluate path loss exponents in large-scale outdoor 802.11 WLANs. In *2009 IEEE 34th Conference on Local Computer Networks* (pp. 348-351). IEEE.

[26] Mawjoud, S.A., 2013. Path loss propagation model prediction for GSM network planning. *International Journal of Computer Applications*, *84*(7).

SciEn
Journal of Engineering Advancements Vol. 04(01) 2023, pp 8-13 https://doi.org/10.38032/jea.2023.01.002

Enhancing Geotechnical Properties of Lateritic Clay with Sawdust Ash-Lime Stabilizer

Oluwafemi O. Omotayo[*], *Oluwapelumi O. Ojuri and Oluwafemi M. Olagunju*

Department of Civil and Environmental Engineering, Federal University of Technology, Akure, Ondo State, Nigeria

Received: January 19, 2023, Revised: March 12, 2023, Accepted: March 13, 2023, Available Online: March 18, 2023

ABSTRACT

One important means of refining the geotechnical characteristics of soils is stabilization. This research sought to improve the geotechnical properties of lateritic clayey soil using sawdust ash-lime (SDAL) stabilizer. Soil-SDAL mixtures were made, after collecting lateritic clay samples and preparing mixtures of lime and sawdust ash in a ratio of 1:2. SDAL mixtures were added to the lateritic clay in increasing percentages from 0 to 10%. The materials' index properties were determined, and compaction of the Soil-SDAL mixtures was done using four compactive efforts namely Reduced British Standard Light (RBSL), Standard Proctor (SP), West African Standard (WAS), and Modified Proctor (MP). Unconfined compressive strength (UCS) tests were performed on the Soil-SDAL mixtures as well. Results of the tests showed that the soil could be classified as an A-7-5(7) soil with a 13.7% plasticity index. The plasticity index increased with the addition of SDAL mixtures up to 6% after which there was a gradual decline. Meanwhile, maximum dry density (MDD) decreased while optimum moisture content (OMC) increased with SDAL addition. Unconfined compressive strength (UCS) of the soil increased from 38.58kN/m^2 at 0% SDAL to a maximum of 129.63kN/m^2 at 6% SDAL, after which there was a gradual decrease. Similar trends were noticed at all compactive efforts, indicating consistency in the performance of the stabilizer. Optimum results were achieved at 6% SDAL content, with Modified Proctor compactive effort giving the maximum value of 1,860kg/m^3 MDD. The results prove that sawdust ash-lime mixture offers tremendous abilities in improving lateritic clay soil properties.

Keywords: Lateritic Clay, Sawdust Ash-Lime, Stabilization, Geotechnical Properties, Compactive effort.

1 Introduction

Soils play an integral role in almost every aspect of civil engineering practice, ranging from road construction to buildings, dams, bridges, etc. Lateritic soils particularly are commonly utilized for various earthwork projects and the construction of road pavement in most tropical nations, including Nigeria, due to their accessibility and inexpensive cost [1]. However, it has been noted that the poor geotechnical characteristics of lateritic soils, which usually act as the major components of sub-grade and base materials, are principal reasons for roadway failure [2]. As a result, it is crucial to apply a variety of stabilizers to enhance the engineering qualities of lateritic soils. In recent times, using waste materials for the purpose of soil stabilization has been gaining popularity. A variety of waste materials have been adapted by researchers for soil stabilization, including waste plastic, ceramic waste, waste fibre, ashes of bio-waste, and others [3]–[5]. Sawdust, a type of wood waste generated from sawmills, constitutes a menace to the environment due to improper disposal. However, when burnt to ashes, the material possesses properties that make it suitable as a potential stabilizer or additive thereby improving the engineering characteristics when combined with lateritic soils. Lime, also, has been noted as a very effective material in soil modification due to its reaction with pozzolanic materials to form cementitious compounds [5]. There are, however, demerits in using lime alone for soil stabilization such as sulphate attack, effects of carbonation, and the negative environmental impact. It is therefore desirable to have a partial substitute material for lime that can aid in mitigating its negative environmental impact while concurrently contributing positively to the strength gain of the soil. This research therefore sought to examine the potential of sawdust ash combined with lime in improving the geotechnical characteristics of lateritic clay.

Lateritic clay soils are a byproduct of weathering from rock or soil components with low concentrations of iron and aluminum oxides or hydroxides [2]. These soils are typically found beneath ferruginous earth crust or hardpan, and mostly have red, reddish-brown, or dark brown color [6]. A warm climate having variations in wet and dry seasons, found commonly in tropical regions, favors laterization [7]. When wet, there is usually no significant swelling or loss of resistance in lateritic clays. However, there is considerable shrinkage when they lose water [8]. In their natural conditions, a number of lateritic clay soils have poor engineering qualities, occasionally exhibiting severe swelling, low strength, excessive plasticity, and a large drop in strength when exposed to water [1].

Sawdust, on the other hand, is wood chippings or waste wood particles gotten from hardwood that has been processed in sawmills. When the sawdust is calcinated, they produce sawdust ashes. If the initial moisture content of this ash is kept within reasonable limits (less than 50%), it can be a viable lightweight fill material with minimal issues during compaction [9]. Typically, sawdust ash has a high concentration of alumina and silica with little lime, as well as a good pozzolanic performance especially when clean sawdust is used [10]. It is a very cheap and widely available material for use since sawdust can be gotten from any local sawmill at very little or no cost. Using sawdust ash also makes possible a better and more economical means of managing waste from the wood industry. This prompted the choice of sawdust ash for use in this study.

Lime (or Calcium oxide), generally referred to as quicklime, is a caustic alkaline solid crystal with a white color at room temperature [9]. When lime reacts with medium-, moderately-,

---

[*]Corresponding Author Email Address: ooomotayo@futa.edu.ng

or fine-grained soils, it improves strength and workability while reducing plasticity [11]. It also reduces the apparent amount of soil fines, by promoting the coalescence and aggregation of clay particles [12]. Generally, when lime interacts chemically with moist clay minerals, the pH rises, increasing the solubility of siliceous and aluminous compounds [13]. It has also been noted that specific soil properties can affect the chemical reaction of lime with soils to produce cementitious materials, some of which include: pH, clay mineralogy, natural drainage, and organic content.

This study aimed at the characterization of lateritic clay, sawdust ash, and lime, and the determination of the compaction and strength characteristics of lateritic clay combined with sawdust ash lime (SDAL) mixtures.

2 MATERIALS AND METHODS

2.1 Study Soil

The lateritic soil sample chosen for this study was taken at a depth of 0.8m from a site located at the Federal University of Technology, Akure (latitude 7˚18`18.48" and longitude 5˚8`20.65"), Ondo State, Nigeria.

2.2 Sawdust Ash

This is an agricultural by-product obtained from the calcination of sawdust gotten from local sawmills in the state. The sawdust used in this study was obtained from a local sawmill at Roadblock, Orita Obele, Akure, Ondo State, Nigeria, and calcinated using a locally made furnace.

2.3 Lime

For the purpose of this study, hydrated lime, $Ca(OH)_2$, was purchased from Pascal Scientific, Akure, Ondo State. The mechanism of action of lime reaction with soil is explained briefly as follows. As soon as the soil is mixed with lime, there are instantaneous changes in the soil's strength, workability, and plasticity index, due to flocculation-agglomeration reaction and cation exchange. After then, cementation produced by carbonation—a reaction between lime and carbon dioxide in cavities in the soil or the open air—occurs, leading to an immediate strength gain. In the long term, the pozzolanic reactions between lime and the clay mineral's silica and alumina result in the development of cementitious products including calcium-silicate-hydrates (C-S-H), calcium-aluminate-hydrates (C-A-H), and calcium-aluminum-silicate-hydrates (C-A-S-H) [14]. These reactions are represented in equations Eq. (1) to Eq. (3):

$$Ca(OH)_2 \rightarrow Ca^{2+} + 2(OH)^- \quad (1)$$

$$Ca^{2+} + OH^- + SiO_2 \text{ (silica from clay)} \rightarrow CSH \quad (2)$$

$$Ca^{2+} + OH^- + Al_2O_3 \text{ (alumina from clay)} \rightarrow CAH \quad (3)$$

2.4 Mix Proportion

In choosing the right chemicals to stabilize soil, certain requirements were prescribed by [11]. Lime was considered appropriate for soils having a plasticity index higher than 10 (PI>10). With soils having their plasticity index falling between a range of 5 – 20, lime fly-ash blends are advised, with the lime addition in a range of 4 – 7% and fly ash (class C type) between limits of 4% and 7%. While combining both lime and fly ash, a range of 1:1 to 1:9 respectively is advised. It is important to note, however, that lime addition to soil depends on the application. For stabilization, 5% to 10% lime is considered appropriate, while 2% to 3% lime by dry weight of soil is acceptable for modification [15]. According to Beeghly [16], for cases of lime and Class F fly ash combination, lime can be added to the Class F fly ash in ratios from 1:2 to 1:4 respectively with satisfactory results. He noted that this combination of lime and fly ash will produce greater strengths than using lime singly.

The combination of sawdust ash with lime is hence expected to produce a more efficient result. Thus, considering the above recommendations, one part of lime was added to two parts of sawdust ash (referred to as SDAL), and then the mixture was added to the lateritic soil in percentages ensuring an even mix. The appropriate amount of soil was combined with SDAL mixes in percentages of 0, 2, 4, 6, 8, and 10% to create the test specimens. Table 1 shows the mixture proportion of the soil-SDAL mixture. The samples of the sawdust ash, lime, sawdust ash lime mixture, and combination of the SDAL with dry lateritic clay are shown in Fig. 1.

Plate 1: Sawdust Ash

Plate 2: Hydrated Lime

Plate 3: Sawdust Ash Lime Mixture (SDAL)

Plate 4: Mixture of SDAL with dry lateritic

Fig. 1 Sawdust Ash, Hydrated Lime, SDAL, and SDAL with dry lateritic clay

Table 1 Mixture percentages of Soil-SDAL

Sample ID	Percentage of SDAL added (%)
LCA	0
SDAL-2	2
SDAL-4	4
SDAL-6	6
SDAL-8	8
SDAL-10	10

2.5 Index Properties

The distribution of the soil's particle size, specific gravities of the soils and sawdust ash, as well as the soil's plasticity characteristics, were determined in accordance with BS1377:Part 2 [17].

2.6 Compaction Test

Four compactive energy levels were employed including Standard Proctor (SP), Modified Proctor (MP), West African Standard (WAS), and Reduced British Standard Light (RBSL). The soil was first dried in an oven and properly ground to pass through the 4.75mm sieve. The Standard Proctor (also known as British Standard Light) and the Modified Proctor (also known as British Standard Heavy), and the Reduced British Standard Light (RBSL) compaction tests were conducted in consonance with BS1377:Part 4 [18]. The reduced British Standard Light (RBSL) is the force produced by a 2.5 kg rammer striking three layers at a distance of 300 mm apart with 13 uniformly distributed blows on each layer [18]. The WAS compaction, which is frequently used in West Africa, involves applying ten (10) blows to each of five layers in a British Standard mold using the force generated by a 4.5 kg rammer falling through a distance of 450 mm [19].

2.7 Unconfined Compressive Strength Test

In accordance with BS1377:Part 7 [20], unconfined compressive strength (UCS) test was conducted on cylinder-shaped specimens of soil-SDAL mixtures 40 mm in diameter and 81 mm in depth. The specimens were placed in a UCS machine and tested under a 1%/min strain rate.

3 Results and Discussions

3.1 Soil-SDA Index Characteristics

Physical characteristics of the soil and sawdust ash are presented in Table 2 while Fig. 2 shows the particle size distribution curve for the lateritic soil. Fig. 3 shows the description of Atterberg limits based on the plasticity characteristics of the soil.

Table 2 Physical Characteristics of Lateritic Soil and Sawdust Ash

S/N	Property	Sieve Mesh Diameter (mm)	LCA
1.	Grain Size Distribution (percent finer than)	4.760	91.35
		2.360	72.92
		1.700	69.86
		1.180	59.27
		0.600	56.14
		0.500	48.38
		0.425	48.34
		0.212	41.73
		0.150	38.93
		0.075	36.91
		0	0
2	Specific Gravity	2.75	1.98

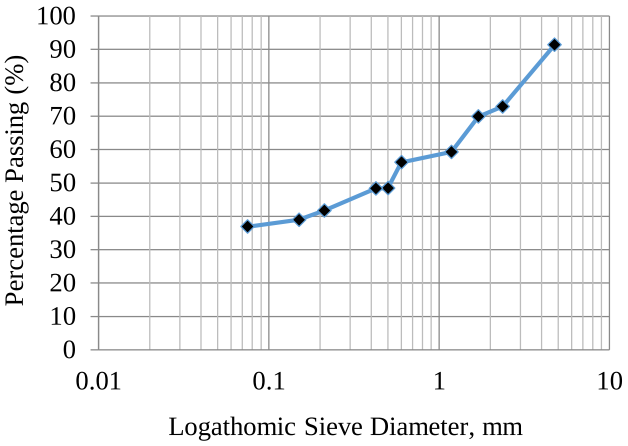

Fig. 2 Particle size distribution for the lateritic soil

Furthermore, Atterberg limit results, including plastic limit (PL), liquid limit (LL), linear shrinkage (LS), and plasticity index (PI) for the specimens of soil-SDAL mixtures are shown in Fig. 3.

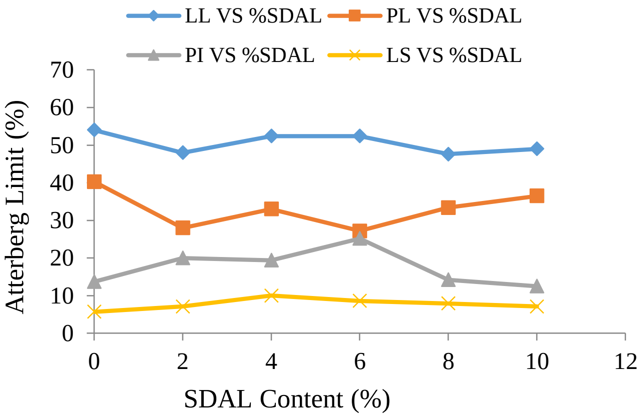

Fig. 3 Comparison of Atterberg limits based on SDAL content

Results from the particle size analysis (Table 1 and Fig. 2) show that the soil contains about 36.78% fines (silt and clay size fraction). The soil has a specific gravity of 2.75, falling within the suitable standard range of 2.60 to 2.80 specified by Wright [21]. Meanwhile, the sawdust ash was found to have a low specific weight with a specific gravity of 1.98. The soil had a plasticity index of 13.7%, with a 54% liquid limit and a 40.3% plastic limit. The soil can thus be classified as an A-7-5(7) soil based on the AASHTO classification system since its plasticity index (PI) ≤ (LL-30).

When the sawdust ash lime mixtures were combined with the soil, a general reduction in the liquid limits (LL) and plasticity indices (PI) was noticed although with slightly inconsistent variations, between a range of 54 and 47.6% for LL, and 20 and 12.5% for PL, for SDAL content from 0 to 10%. This is seen in Fig. 3. There was also a sudden increase of PI at 6% SDAL after which there was a reduction. The PL gradually increased with 6 to 10% SDAL content. This demonstrates how the lateritic clay soil lost its plasticity after being treated with a sawdust ash lime mixture. This occurrence could be a result of the changing soil texture due to the flocculation and aggregation of clay particles induced by the sawdust ash-lime combinations [22]. The values of linear shrinkage were initially 5.7 and 7.1% at 0 and 2% SDAL content, but later showed a marked reduction with an increase in

SDAL content from 4 to 10% SDAL content, with linear shrinkage values of 10.0, 8.6, 7.9 and 7.1% respectively.

In a research conducted by Raheem and Suleiman [23], results for the chemical composition of sawdust ash showed an average percentage composition of $SiO_2 + Al_2O_3 + Fe_2O_3$ to be 74.89% and CaO to be 4.21%. Hence, sawdust ash can be classified as Class F fly ash, having satisfied the 70% minimum condition for pozzolans in accordance with ASTM C618 [24] and Jerath and Hanson [25]. With CaO content lower than 10% and a low potential for pozzolanic reaction, Reimer [26] noted that Class F fly ash is not effective as a stabilizing agent by itself. However, in the presence of lime or cement, fly ash turns will be very efficient for stabilization. As a result, it can be argued that the sawdust ash in this case serves both as a filler and a major contributor to the pozzolanic reaction that is brought about by the mixture of soil and lime.

3.2 Compaction Characteristics

Fig. 4 and Fig. 5 shows the variations of MDD and OMC with SDAL content added to the soil.

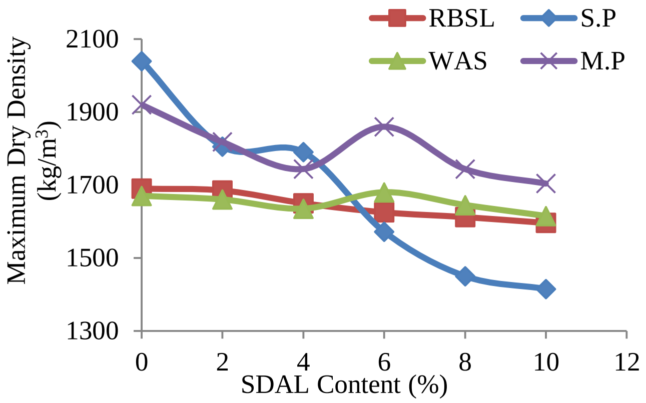

Fig. 4 Comparison of maximum dry Density based on SDAL content

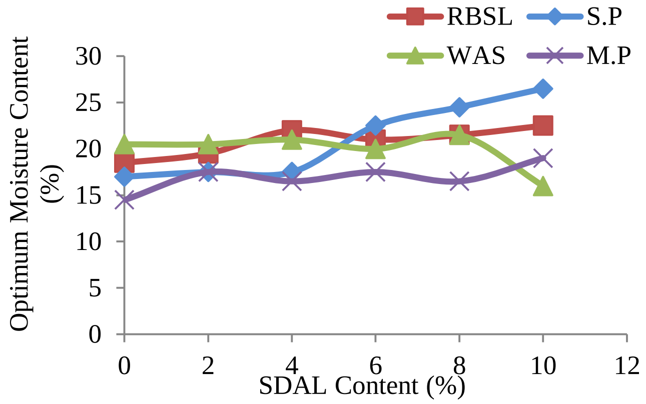

Fig. 5 Comparison of optimum moisture content based on SDAL addition

As shown in Fig. 4, a decreasing trend was noticed with the MDD values of the compacted soil-SDAL mixtures within the ranges of 1,690kg/m^3 to 1,596kg/m^3 for Reduced British Standard Light compactive effort, 2,040kg/m^3 to 1,415kg/m^3 for Standard Proctor, 1,670kg/m^3 to 1615kg/m^3 for West African Standard, and 1,920 kg/m^3 to 1,704kg/m^3 for Modified Proctor compactive effort. While there was an overall reduction in MDD for all compactive efforts, it was specifically observed that there was a sharp sudden increase at 6% SDAL content for Modified Proctor and West African Standard efforts, before a later reduction.

At 6% SDAL content, the highest MDD values were obtained for the four compactive efforts, with values of 1,625 kg/m^3, 1,572 kg/m^3, 1,680 kg/m^3 and 1,860 kg/m^3 for Reduced British Standard Light, Standard Proctor, West African Standard, and Modified Proctor compactive efforts respectively (Fig. 4). The sawdust ash's lower specific gravity, the flocculation and aggregation of clay particles brought on by cation exchange, which increased volume and generated a commensurate decline in dry densities, are possible causes of the fall in the dry unit weight. The rise in the OMC, on the other hand, could be explained by the sawdust ash lime's larger surface area and the additional water required for hydration [19], [22], [27]–[30]. Several studies have noticed a similar pattern [9], [22], [29].

On the other hand, the OMC showed an increasing trend with an increasing percentage of SDAL content (from 0% to 10%), with values between 17.0 and 26.5% for the Standard Proctor (S.P) compactive effort, 16.5 and 21.5% for the West African Standard (WAS) compactive effort, and 14.5 and 19.0% for Modified Proctor (M.P) compactive effort as shown in Fig. 5. However, while there was an initial increase in OMC for the Reduced British Standard Light (RBSL) compactive effort, there was a sudden drop at 6% SDAL content to 21% and latter increase to 22.5% at 10% SDAL content.

3.3 Unconfined Compressive Strength

Fig. 6 shows the effect of SDAL content on the unconfined compressive strength, while Fig. 7 represents the stress-strain curve of the lateritic soil based on SDAL content.

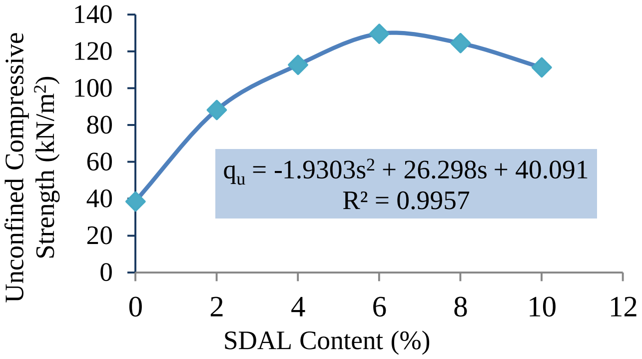

Fig. 6 Effect of SDAL content on unconfined compressive strength

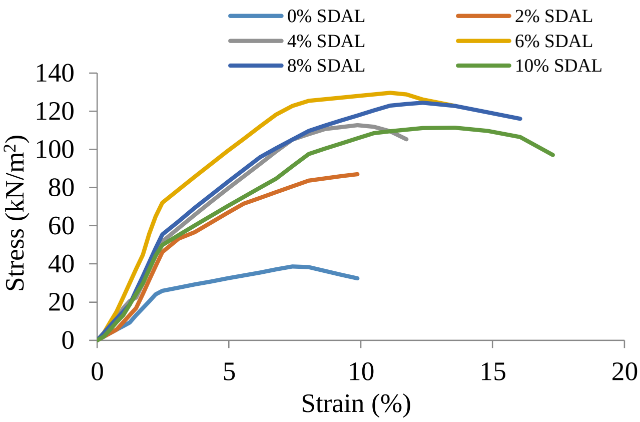

Fig. 7 Soil stress-strain curve relationship based on SDAL content

As seen in Fig. 6, the unconfined compressive strength of the natural lateritic soil sample was 38.58kN/m^2. When SDAL was added, UCS values increased with SDAL content to a maximum value of 129.63kN/m^2 at 6% SDAL content, after which there was a gradual decrease in the UCS value till 10% SDAL content. The stress-strain curve in Fig. 7 also shows that the addition of sawdust ah lime mixtures to the soil improves the elastic properties as well as the strength of the soil. The natural lateritic soil was able to withstand low stress and strain. However, with the addition of SDAL, the treated soil showed higher strength and strain at failure compared to that of the untreated soil. A similar pattern was observed by [31], and the strength improvement can be attributed to the pozzolanic reaction between the sawdust ash lime and the soil constituents. The variation of the unconfined compressive strength of the soil-SDAL mixtures, as described in Fig. 6, can be represented by the polynomial Eq. (4), with a coefficient of determination value of 0.9957.

$$q_u = -1.9303s^2 - 26.298s + 40.091 \tag{4}$$

Where q_u represents unconfined compressive strength, and s represents the percentage of SDAL added.

3.4 Comparison of Compaction Characteristics of Soil-SDAL Mixtures at 6% SDAL

At the optimum value of 6% SDAL, a comparison of the values of maximum dry densities for all four compactive efforts is presented in Fig. 8.

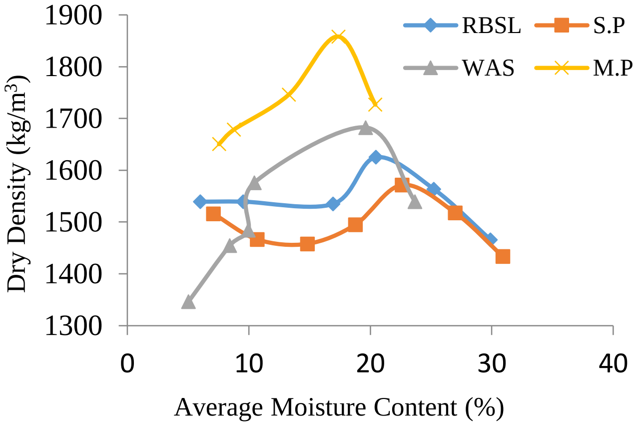

Fig. 8 Compaction test results for SDAL-6

Optimum strength values were achieved at 6% SDAL content, using Modified Proctor compactive effort with the maximum value of 1,860kg/m^3 MDD. The maximum unconfined compressive strength value obtained was 129.63kN/m^2, indicating an increase in strength over 200 percent (236 percent) compared to that of the natural lateritic soil sample (LCA). This result amply demonstrates the efficiency of the sawdust-ash lime combinations when applied at this optimum value.

4 Conclusion

This study was carried out as an initial evaluation with the goal of improving the geotechnical properties of lateritic clay with sawdust ash-lime mixtures for engineering applications. Test specimens were made by combining lime and sawdust ash in a 1:2 ratio, after which the mixtures were combined with the soil at increasing percentages of 2% from 0 to 10% SDAL. Following SDAL treatment, index characteristics of the lateritic clay improved with a decrease in plasticity index and a rise in linear shrinkage. It was also observed that there was a reduction in MDD decreased while OMC increased with higher SDAL content. The maximum value of MDD and least OMC was obtained with the Modified Proctor Effort, making it the most preferred method of compaction for promising results. A Peak UCS value of 129.63kN/m^2 was obtained at 6% SDAL addition, after which there was a falling trend. With over 200% increase in the soil's UCS value, 6% optimum SDAL content is advised. With compaction, higher UCS values can yet be achieved. This study demonstrates that using this agro-industrial/chemical mixture significantly improves the engineering qualities of lateritic clay soil and offers an efficient approach to handling agro-industrial by-products rather than disposal, which could cause environmental issues.

Further investigation using increased lime content in the SDAL ratio, and the suitability of other additives is proposed. Moreover, this mixture can also be investigated for its suitability in landfill liners.

Declaration of Interest

The authors declare no conflict of interest.

References

[1] Ogundalu, A.O., Adeboje, A.O. and Adelaja, F., 2014. Effects of Soldier-Ant Mound (SAM) on the strength characteristics of lateritic clay soils. *British Journal of Applied Science & Technology*, *4*(10), p.1554.

[2] Amu, O.O., Bamisaye, O.F. and Komolafe, I.A., 2011. The suitability and lime stabilization requirement of some lateritic soil samples as pavement. *Int. J. Pure Appl. Sci. Technol*, *2*(1), pp.29-46.

[3] Mali, S., Kadam, S., Mane, S., Panchal, K., Kale, S. and Navkar, Y., 2019. Soil stabilization by using plastic waste. *Int. Res. J. Eng. Technol.(IRJET)*, *6*, pp.4056-4060.

[4] Upadhyay, A. and Kaur, S., 2016. Review on soil stabilization using ceramic waste. *Int. Res. J. Eng. Technol*, *3*(07), pp.1748-1750.

[5] Afrin, H., 2017. A review on different types soil stabilization techniques. *International Journal of Transportation Engineering and Technology*, *3*(2), pp.19-24..

[6] Huat, B.B., Gue, S.S. and Ali, F.H., 2004. Slope failures in tropical residual soils. In *Tropical Residual Soils Engineering* (pp. 142-194). CRC Press.

[7] Ushie, F.A. and Anike, O.L., 2011. Lateritic weathering of granite-gneiss in Obudu Plateau, south eastern Nigeria. *Global Journal of Geological Sciences*, *9*(1), pp.55-73.

[8] Boscov, M.E.G., Hachich, W.C., Mahler, C.F. and de Oliveira, E., 2011. Properties of a lateritic red soil for pollutant containment. *Journal of Environmental Protection*, *2*(07), p.923.

[9] Rao, K.D., Anusha, M., Pranav, P.R.T. and Venkatesh, G., 2012. A laboratory study on the stabilization of marine clay using saw dust and lime. *Ijesat] Int. J. Eng. Sci. Adv. Technol*, *2*(4), pp.851-862.

[10] Ogunribido, T.H.T., 2012. Geotechnical properties of saw dust ash stabilized southwestern Nigeria lateritic

soils. *Environmental Research, Engineering and Management*, *60*(2), pp.29-33.

[11] I. D. of T. (INDOT), “Design procedures for soil modification or stabilization,” *Indiana Dept. of Transportation*, 2002.

[12] Makusa, G.P., 2013. Soil stabilization methods and materials in engineering practice: State of the art review. Department of Civil, Environmental and Natural resources engineering, Division of Mining and Geotechnical Engineering, Luleå University of Technology, Luleå, Sweden.

[13] Mallela, J., Quintus, H.V. and Smith, K., 2004. Consideration of lime-stabilized layers in mechanistic-empirical pavement design. *The National Lime Association*, *200*(1), pp.1-40.

[14] Solanki, P. and Zaman, M., 2012. Microstructural and mineralogical characterization of clay stabilized using calcium-based stabilizers. In *Scanning electron microscopy*. IntechOpen.

[15] Maher, M., Marshall, C., Harrison, F. and Baumgaertner, K., 2005. *Context sensitive roadway surfacing selection guide* (No. FHWA-CFL/TD-05-004). United States. Federal Highway Administration. Central Federal Lands Highway Division.

[16] Beeghly, J.H., 2003, October. Recent experiences with lime-fly ash stabilization of pavement subgrade soils, base and recycled asphalt. In *Proceedings of the International Ash Utilization Symposium, University of Kentucky, Lexingston, USA, Oct* (pp. 20-22).

[17] Standard, B., 1990. 1377:2. *Methods of test for soils for civil engineering purposes,” British Standard Institution, London*.

[18] Standard, B., 1990. 1377:4. *Methods of test for soils for civil engineering purposes,” British Standard Institution, London*.

[19] Osinubi, K.J., Eberemu, A.O. and Amadi, A.A., 2009. Compacted lateritic soil treated with blast furnace slag as hydraulic barriers in waste containment systems. *International Journal of Risk Assessment and Management*, *13*(2), pp.171-189.

[20] Standard, B., 1990. 1377 (1990) Methods for test for civil engineering purposes. *British Standard Institute, London*.

[21] Wright, P.H. and Paquette, R.J., 1987. *Highway engineering*. John Wiley & Sons, Incorporated.

[22] Amadi, A.A., 2012. Utilisation of fly ash to improve the engineering properties of lateritic soil. *International Journal of Materials Engineering Innovation*, *3*(1), pp.78-88.

[23] Raheem, A.A. and Sulaiman, O.K., 2013. Saw dust ash as partial replacement for cement in the production of sandcrete hollow blocks. *International Journal of Engineering Research and Applications*, *3*(4), pp.713-721.

[24] A. ASTM C618, “Standard specification for coal fly ash and raw or calcined natural pozzolan for use in concrete,” *ASTM international*, 2019.

[25] Jerath, S. and Hanson, N., 2007. Effect of fly ash content and aggregate gradation on the durability of concrete pavements. *Journal of materials in civil engineering*, *19*(5), pp.367-375.

[26] D. J. Reimer, “Military Soils Engineering,” Field Manual Headquarters, Department of the Army. Washington, DC., 1992.

[27] Oriola, F.O.P. and Moses, G., 2011. Compacted black cotton soil treated with cement kiln dust as hydraulic barrier material. *American Journal of Scientific and Industrial Research*, *2*(4), pp.521-530.

[28] Osinubi, K.J. and Eberemu, A.O., 2013. Hydraulic conductivity of compacted lateritic soil treated with bagasse ash. *International Journal of Environment and Waste Management*, *11*(1), pp.38-58.

[29] Deb, T. and Pal, S.K., 2014. Effect of fly ash on geotechnical properties of local soil-fly ash mixed samples. *Int. J. Res. Eng. Technol*, *3*(5), pp.507-516.

[30] Ojuri, O.O. and Oluwatuyi, O.E., 2018, May. Compacted sawdust ash–lime-stabilised soil-based hydraulic barriers for waste containment. In *Proceedings of the Institution of Civil Engineers-Waste and Resource Management* (Vol. 171, No. 2, pp. 52-60). Thomas Telford Ltd.

[31] Butt, W.A., Gupta, K. and Jha, J.N., 2016. Strength behavior of clayey soil stabilized with saw dust ash. *International Journal of Geo-Engineering*, *7*, pp.1-9.

SciEn
Journal of Engineering Advancements Vol. 04(01) 2023, pp 14-18 https://doi.org/10.38032/jea.2023.01.003

Determination of Parameters of Linear Quadratic Regulator using Global Best Inertia Weight Modified Particle Swarm Optimization Algorithm

*Agbroko Oghenenyoreme Emakpo**, *Ogunti Erastus Olarewaju*

Department of Electrical and Electronics Engineering, Federal University of Technology, Akure, Ondo State, Nigeria

Received: January 31, 2023, Revised: March 13, 2023, Accepted: March 15, 2023, Available Online: March 20, 2023

ABSTRACT

The characteristics of a linear Quadratic Regulator (LQR) are hinged upon two parameters and they are, the state weighting matrix Q and the Control weighting matrix R. In this study Global Best Inertia Weight modified variant of the particle swarm optimization algorithm was used to determine these two important parameters of an LQR which was then used to control a bus suspension system. The evaluation of the open loop and closed loop showed that the closed loop system attained a steady state in a time of 350.36 seconds compared to the open loop system (47,734.3 seconds) when both systems were subjected to pot hole (step) signal.

Keywords: Linear Quadratic Regulator (LQR), Bus Suspension, Road Profile, Global Best Inertia Weight Modified Particle Swarm Optimization (GBbest IWM PSO) Algorithm.

1 Introduction

LQR is a type of linear optimal control that is based on a state space representation model. It is used for multivariate dynamic systems [1]. It generates a control law by utilizing feedback from its output with its derivatives [2]. Its performance or behaviour, is determined by the state weighting matrix Q and the control weighting matrix R [3]. The values of Q and R, are traditionally ascertained by trial-and-error method [3], and using traditional control methods can be so laborious that at times, it can be so difficult to achieve the best parameters [4], [5], [6]. Due to the aforementioned reason, researchers used various evolutional algorithms such as particle swarm optimization (PSO) algorithm, Bees algorithm, and Ant Colony among others, to determine the weighting parameters Q and R of an LQR [4]. PSO is an Optimization algorithm which is the result of research by Dr. Russell Eberhart and James Kennedy in 1995 [7]. It is a computational method based on the idea of collective conduct and swarming of populations inspired by the social attitude of bird flocking and fish schooling [8]. The merits of PSO are that it is simple and easy to apply and has quick convergence [9]. It, however, has a disadvantage in that, its particles are sometimes trapped in a local minimum instead of the global minimum, at the later part of convergence thus the final value ends up being a local minimum instead of a global minimum. For this reason, researchers have come up with various modified variants of PSO which include: Discrete PSO, Guaranteed Convergence PSO, Regrouping PSO, Neighborhood Guaranteed Convergence PSO, Niche PSO, Neighborhood search PSO, Immunity-Enhanced PSO, Quantum-Behaved PSO, Multi-Objective Optimization PSO, Hybrid PSO among others. These are meant to raise the diversity of particles and enhance convergence performance [10].

This research used the Global best inertia weight modified variant of PSO (Gbest IWM PSO) to determine the parameters of LQR to control a Bus suspension system.

2 Concept and Review of Related works

The aim of designing and controlling a system with LQR is to return the system to an equilibrium whenever it is displaced from equilibrium in such a way as to minimize a performance index [11]. A performance index is referred to as the addition of deviations of key measurements from their desired state or values. To find the optimal gain, the performance index is first defined and then the solution of the resulting Algebraic Riccati Equation (ARE) is obtained [12]. In this research, we sort to use LQR to control a bus suspension system so that whenever the suspension system is subjected to a road disturbance, it dampens out oscillations as quickly as possible. A suspension system is a device that isolates the body of an automobile from its wheels [13]. It is made up of linkages, damper, and springs that connect a bus to its wheels as shown in Fig. 1.

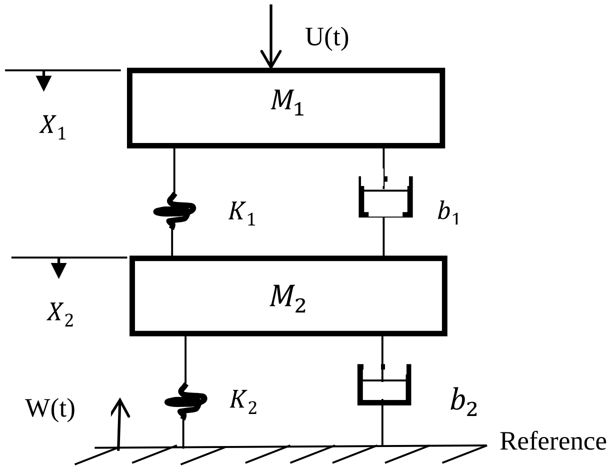

Fig. 1 Diagram of a vehicle suspension system

It is used to decrease the vertical acceleration transmitted to occupants (fare payers and driver) of an automobile. The suspense is designed to provide road handling capacity, load carrying capacity, and passenger comfort.

---

*Corresponding Author Email Address: everestagbroko@gmail.com

Published by: SciEn Publishing Group

Three types of automobile suspense exist and are active, semi active, and passive. The passive system consists of passive elements such as springs and a damper (shock absorber) [13], [14], [15], [16]. It stores energy by means of springs and dissipates them through the damper. The active system stores, dissipates, and introduces energy into the system. While the active system can be seen as a closed loop system, the passive is an open loop system. The semi active system is a compromise of both the active and passive systems. It doesn't introduce power into the system and hence cannot make the system to be unstable, unlike active suspense.

The bus suspension block diagram shown in Fig. 1 comprises of mass M_1, which is a quarter of the automobile body mass, also referred to as the sprung mass while mass M_2 is the mass of tires and wheels, also referred to as the unsprung mass, K_1 and K_2 are the spring constant of sprung and unsprung mass respectively, b_1 and b_2 are the damping constant of sprung and unsprung mass respectively, W(t) represents the road disturbance, X_1 and X_2 are the system output while U(t) is the actuating signal. See Table 1.

In PSO, every particle is a prospective solution in the search space [7]. Their movement is determined by two key elements: first is the individual particle's best position and second, the global best position, which is the overall best position that has been generated by the entire particle (swarm). The velocity and position of each particle are updated for each iteration, using Eq. (1) and Eq. (2).

$$V_i^{t+1} = V_i^t + C_1 * rand_1 * (P_{ibest} - X_i^t) + C_2 * rand_2 * (G_{best} - X_i^t) \quad (1)$$

$$X_i^{t+1} = X_i^t + V_i^{t+1} \quad (2)$$

Where V_i^{t+1} is the present particle velocity, V_i^t is the previous particle position, X_i^{t+1} is the present particle position, X_i^t is the previous particle position, P_{ibest} is the particle's best position, G_{best} is the Global best position, C_1 and C_2 are personal and social acceleration coefficients respectively, $rand_1$ and $rand_2$ are random variables between one and four.

To improve control on the scope of the search, Shi and Eberhart introduced inertia weight (W) in 1998 [17] and the updated velocity value is shown in Eq. (3).

$$V_i^{t+1} = W * V_i^t + C_1 * rand_1 * (P_{ibest} - X_i^t) + C_2 * rand_2 * (G_{best} - X_i^t) \quad (3)$$

Further, Arumugan & Rao, in 2006, proposed the Gbest IWM PSO algorithm [18] in which, instead of W being a constant, as seen in Eq. (3) and stipulated by Shi and Eberhart, it was made to be dependent on the values of particle best and global best position for each iteration as shown in Eq. (4).

$$W_i = (1.1 - \frac{G_{best}}{P_{ibest}}) \quad (4)$$

3 Methodology

Based on the diagram of a bus suspension model in Fig. 1 and Newton's law of motion two equations can be derived. They are:

$$U(t) = M_1\ddot{X}_1 + b_1(\dot{X}_1 - \dot{X}_2) + k_1(X_1 - X_2) \quad (5)$$

$$W(t) = M_2\ddot{X}_2 + b_2\dot{X}_2 + b_1(\dot{X}_2 - \dot{X}_1) + k_2X_2 + k_1(X_2 - X_1) \quad (6)$$

Table 1 Bus suspense parameters (source [19])

Symbol	Parameter	Value/unit
M_1	A quarter of the bus body mass	2,500 kg
M_2	Unsprung mass (tire and wheel)	320 kg
k_1	Spring coefficient of the suspension system	80,000 N/m
k_2	Spring coefficient of wheel and tire	500,000 N/m
b_1	Damping coefficient of the suspension system	350 N.s/m
b_2	Damping coefficient of tire and wheel	15,020 N.s./m

W(t) represents the road disturbance and u(t) is the actuating signal. The state space model of the system was then designed from the state space equations. Consider a representation of the linear time invariant (LTI) system shown in Fig. 2.

$$\dot{x} = Ax + Bu \quad (7)$$

$$y = Cx + DU \quad (8)$$

Where A is n x n state matrix, B is n x r input matrix, C is m x n output matrix, D is m x r direct transmission matrix, x is n x 1 state vector, y is m x 1 output vector and u is r x 1 input vector.

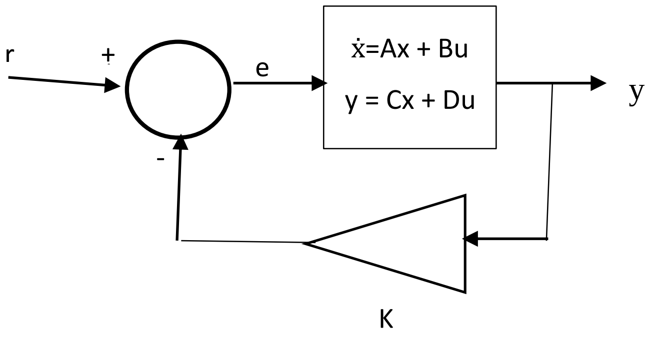

Fig. 2 Block diagram of LTI system.

The cost function of a linear Quadratic regulator is:

$$J = \frac{1}{2}\int_{t_0}^{t_f} (x^T Qx + u^T Ru)dt \quad (9)$$

Where Q is a positive semi-definite nxn matrix called the State weighting matrix and R is a positive definite matrix that is called the control weighting matrix. The aim of an LQR design is to achieve an optimal control input u* that will minimize the cost (objective) function as t_f tends to infinity.

$$u^* = -Kx(t) \quad (10)$$

$$K = R^{-1}B^T P \quad (11)$$

Where K is the optimal control feedback matrix and P is the solution of the ARE which is

$$PA + A^T P + Q - PBR^{-1}B^T P = 0 \quad (12)$$

The performance Index used for this research is Integral Time Absolute Error ie

$$ITAE = \int /e/ dt \quad (13)$$

Where e from Fig. 2, is the error signal, given as:

$$e = r - ky \tag{14}$$

r is the reference input and y is the system output.

The plant was designed in MATLAB SIMULINK using MATLAB 2020b version, while the Gbest IWM PSO algorithm was coded on the EDITOR window by applying the chosen performance index (ITAE) as its objective function with its parameters indicated in Table 2. The PSO variant was set to run for fifty iterations and the Global best position was recorded. With the aid of the MATLAB "To Workspace" block and MATLAB "sim" command, the Simulink model and the EDITOR were able to interact and results were recorded. Utilizing Eqs. (11) and (12), the values of P, Q, and R were derived.

Table 2 Gbest IWM PSO parameters

S/N	Item	Value	Unit
1	C_1	2	Constant
2	C_2	2	Constant
3	n	4	Number
4	vsize	[1 n]	1xn matrix
5	pop	100	Number
6	minvar	-10000	Meter
7	maxvar	100000	Meter
8	Maximum velocity	22000	m/s
9	Minimum velocity	-22000	m/s

Where n is the number of decision variables, vsize is the matrix size of decision variables, pop is the particle population, minvar is the lower bound of the particles, and maxvar is the upper bound of the particles.

The designed LQR controlled system was then subjected to test signals and the outputs were recorded.

Test signals: Two different types of test signals representing two road conditions were utilized for this study. They can be referred to as road profiles, road disturbances, or road conditions. They are:

Step input- this was modeled to emulate a pot-hole condition of roads. It can be better understood when seen as a vehicle coming out of a pot hole. Fig. 3.

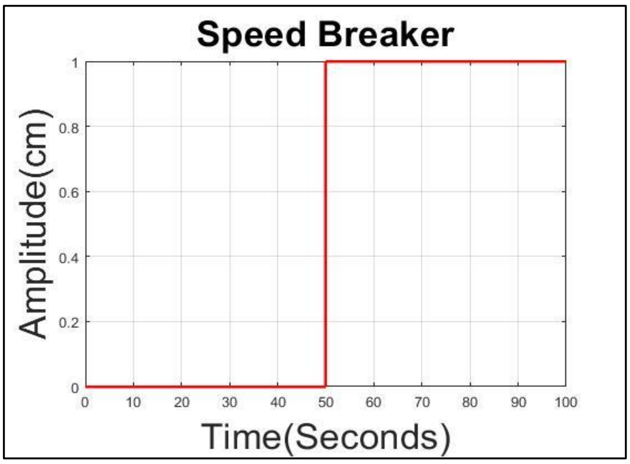

Fig. 3 Step signal

Road Bump or Speed breaker- this is a combination of step input, product block, and sine wave (Fig. 4) to produce the signal shown in Fig. 5 [14].

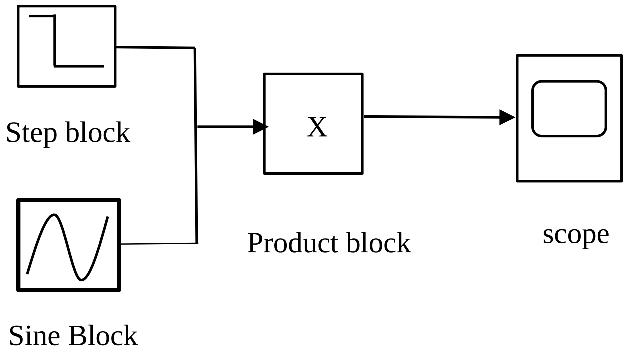

Fig. 4 Design layout of speed breaker

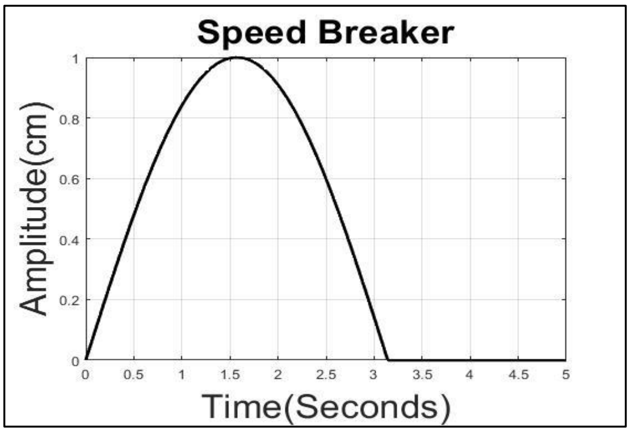

Fig. 5 Speed breaker signal

4 Results and Discussion

The following are the simulation results:

Gbest = [73326 74138 5757 83650], $R = \frac{1}{17.9413} \times 10^{-8}$

$$p = \begin{bmatrix} 6.51 & 0.1567 & -26.1942 & 0.0201 \\ 0.1567 & 106.5042 & -1.363 & -12.5524 \\ -26.1942 & 1.1363 & 187.4036 & 0.0202 \\ 0.0201 & -12.5524 & -0.0202 & 103.1717 \end{bmatrix},$$

$$Q = \begin{bmatrix} 0 & 0 & 0 & 0 \\ 0 & 3 & 0 & 0 \\ 0 & 0 & 0 & 0 \\ 0 & 0 & 0 & 10 \end{bmatrix}$$

The open loop system response is shown in Fig. 6, while Fig. 7 shows the step response of the LQR controlled closed loop. Fig. 8 and Fig. 9 give the system's response to bump input. Fig. 10 and Fig. 11 show the pole locations of the open and closed loop systems in graphical form.

The system response consists of deflection and velocity due to the sprung and unsprung mass. For the deflection of sprung mass, the open loop system attained a maximum peak to trough value of 0.0000289cm to 1.9632×10^{-7}cm at a time of 19.51 seconds and 37.05 seconds respectively, a rise time of 9.95secs and a settling time of 47,734.3secs with a steady state value of 0.00001443 cm. For the velocity of sprung mass, the open loop system has a maximum peak to trough value of 2.4028×10^{-6} to -2.39399×10^{-6} cm/s with a peak time of 9.477 seconds and trough time of 28.726 secs and settling time of 35,000 secs. As regards the deflection of unsprung mass, the maximum peak value was 4.04471×10^{-6} cm/s, maximum trough value was

3.51567×10^{-8} cm/s with a peak time of 18.74 secs, trough time of 39.478 secs, and settling time of 33,357.21 secs. For the velocity of unsprung mass, the maximum peak to trough was 3.63609×10^{-7} cm/s to -3.54501×10^{-7} cm/s, peak and trough times of 8.34 and 29.004 secs respectively, and a settling time of 20,000 seconds (See Fig. 6).

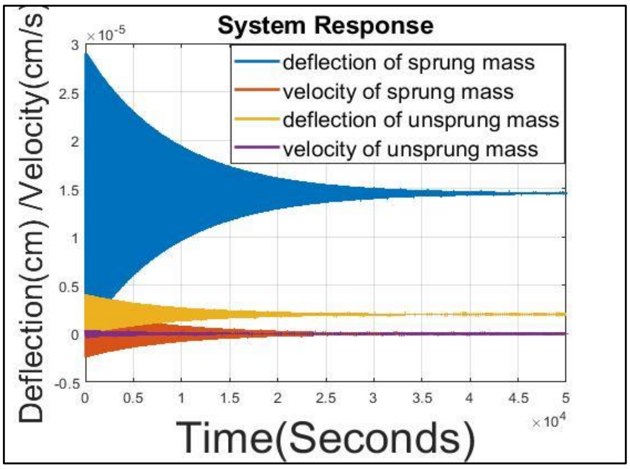

Fig. 6 Open loop system step response.

For closed loop response to pothole signal, as shown in Fig. 7, as regards deflection of sprung mass, the maximum peak to trough value was 1.74477 to 0.444732 cm, the peak time of 19.02 secs, trough time of 37.35 secs, the rise time of 9.94 secs, settling time of 350.36 secs with a steady state value of 1cm. For the velocity of sprung mass, the maximum peak to trough was 0.143799 cm/s to -0.107065 cm/s, peak and trough times of 9.52 and 28.72 secs respectively, settling time of 341.33 secs with a steady state value of 0. As regards the deflection of unsprung mass, the maximum peak to trough was 0.243473 to 0.0601832 cm with a peak time of 18.75 secs, trough time of 37.98 secs, and settling time of 351.3 secs. While for the velocity of unsprung mass, the maximum peak was 0.0224102 cm/s at a time of 8.24 secs, the maximum trough of -0.0162871 cm/s at a time of 28.97 secs and a settling time of 351.3 secs.

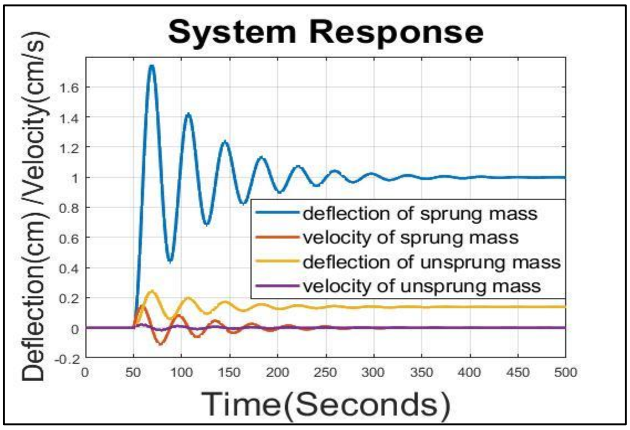

Fig. 7 LQR controlled system step response.

As shown in Fig. 8, with regards to the system open loop response, the deflection of sprung mass attained a maximum peak of 4.7708×10^{-6} cm, maximum trough value of -4.74961×10^{-6} cm, the peak time of 11.04 secs, trough time of 29.56 secs, and settling time of 42,281.1 secs. For the velocity of sprung mass, the maximum peak was 7.66769×10^{-7} cm/s, the maximum trough of -7.89802×10^{-7} cm/s, the peak time of 3.057 secs, trough time of 20.517 secs, and settling time of 40,000 secs. Furthermore, for the deflection of unsprung mass, the maximum peak to trough was 6.98899×10^{-7} to -6.87874×10^{-7} cm/s at a peak time of 10.001 secs, trough time of 30.301 secs, and settled at 35,000 secs. For the velocity of unsprung mass, the maximum peak was 1.70288×10^{-7}cm/s, maximum trough value was -1.5608×10^{-7} cm/s, the peak time of 3.8544 secs, trough time of 20.214 secs, and settling time of 32,500 secs.

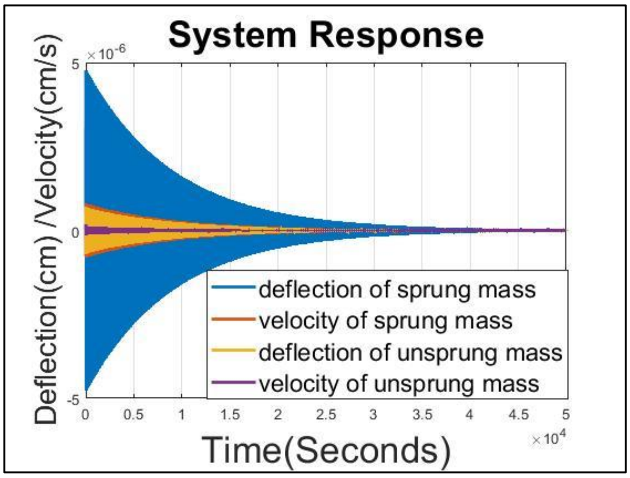

Fig. 8 Open loop bump response.

As shown in Fig. 9, which is the closed loop response to the speed breaker, as regards deflection of sprung mass, the maximum peak was 4.15357×10^{-6} cm, maximum trough of-3.11115×10^{-6} cm, peak time of 10.12 secs, trough time of 29.54secs and settling time of 347.73secs. With reference to the velocity of sprung mass, the maximum peak was 7.33138×10^{-7}cm/s, maximum trough of-6.0146×10^{-7}cm/s, the peak time of 3.01 secs, trough time of 19.25 secs, and settling time of 313.67 secs. For the deflection of unsprung mass, the maximum peak was 6.20629×10^{-7} cm at a time of 10.11 secs, the maximum trough value was -4.57009×10^{-7} cm at a time of 30.29 secs and a settling time of 306.42 secs. Finally, as regard the velocity of unsprung mass, the maximum peak was 1.63343×10^{-7} cm/s, the maximum trough was -1.28999×10^{-7} cm/s, the peak time of 3.82 secs trough time of 20.22 secs, and settling time of 291.303 secs.

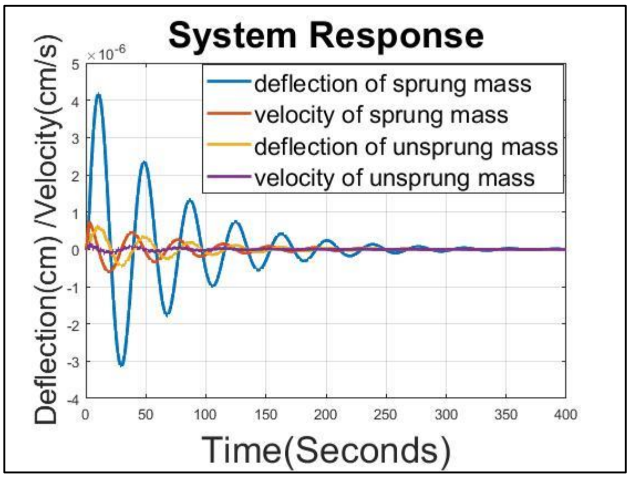

Fig. 9 LQR controlled system bump response.

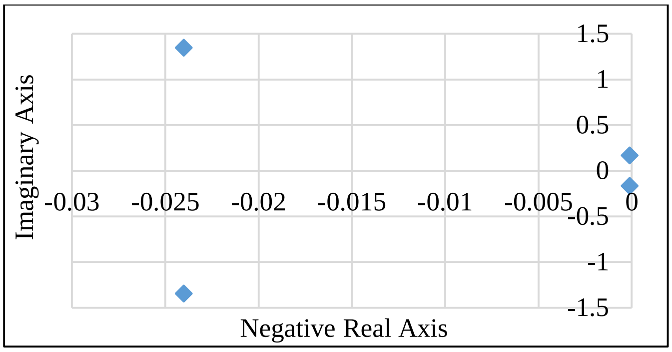

Fig. 10 Open loop system pole location.

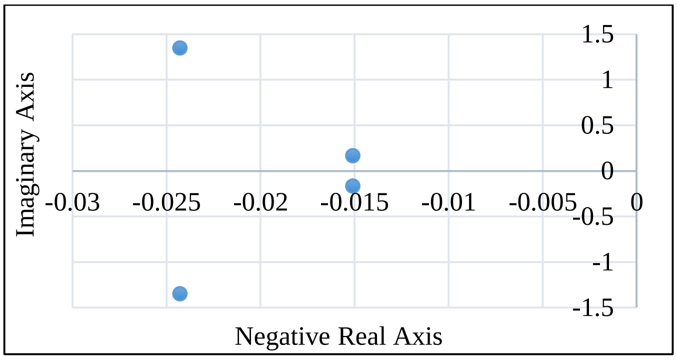

Fig. 11 LQR controlled system pole Location.

From Fig. 10 the open loop pole locations are -0.024 ± j1.3477 and -0.0001 ± j0.1659 while that of the closed loop are at -0.024 ± j1.3478 and -0.0151 ± j0.1652 (Fig. 11). As can be observed, there was a significant relocation of the dominant poles further away from the origin of the s-plane which resulted in a reduction of the system oscillation. Hence the closed loop system damps out oscillation in a shorter duration (350.36 seconds) compared to the open loop (over 47,734.3 seconds) when the systems are subjected to step response. Also, when the system was subjected to a speed breaker, the open loop attained a steady state at about 42,281.1 seconds while the closed loop system attained it at 347.73 seconds considering the deflection of sprung mass only.

5 Conclusion

This research applies Gbest IWM PSO to determine the parameters of an LQR to control a bus suspension system and not a comparison with any other method. However, comparing the open loop system with the closed loop shows significant improvement in the output in terms of reduction in the number of oscillations and settling time due to a drastic relocation of the dominant system poles (-0.0001 ± j0.1659) farther away from the origin of s-plane (Fig. 10 and Fig. 11). The reduction in the number of oscillation and shorter settling time translates into comfort for the occupants of the automobile.

References

[1] Nath, V. and Mitra, R., 2014. Robust pole placement using linear quadratic regulator weight selection algorithm. *Indian Institute of Technology, Roorkee*, *3*, pp. 329-333.

[2] Anderson, B. & Moore, J., 1989. *Optimal control: linear quadratic methods*, Sydney: Prentice-Hall.

[3] Al-Mahturi, A. and Wahid, H., 2017. Optimal tuning of linear quadratic regulator controller using a particle swarm optimization for two-rotor aerodynamical system. *International Journal of Electronics and Communication Engineering*, *11*(2), pp. 196-202.

[4] Önen, Ü., Çakan, A. and İlhan, İ., 2017. Particle Swarm Optimization Based LQR Control of an Inverted Pendulum. *Engineering and Technology Journal*, *2*(5), pp. 168-174.

[5] Sen, M.A. and Kalyoncu, M., 2016. Optimal tuning of a LQR controller for an inverted pendulum using the bees algorithm. *J Autom Control Eng*, *4*(5), pp. 384-387.

[6] Hamidi, J., 2012. Control system design using particle swarm optimization (PSO). *International Journal of Soft Computing and Engineering*, *1*(6), pp. 116-119.

[7] Eberhart, R. and Kennedy, J., 1995, October. A new optimizer using particle swarm theory. In *MHS'95. Proceedings of the sixth international symposium on micro machine and human science* (pp. 39-43). IEEE.

[8] Abdel-Kader, R.F., 2011. Fuzzy particle swarm optimization with simulated annealing and neighborhood information communication for solving TSP. *International Journal of Advanced Computer Science and Applications*, *2*(5), pp. 15-21.

[9] Ahmed, H. and Glasgow, J., 2012. Swarm intelligence: concepts, models and applications. *School Of Computing, Queens University Technical Report*.

[10] Kumar, A., Singh, B.K. and Patro, B.D.K., 2016. Particle swarm optimization: a study of variants and their applications. *International Journal of Computer Applications*, *135*(5), pp. 24-30.

[11] Burns, R., 2001. *Advanced control engineering*. Elsevier.

[12] Alias, N.A., 2013. *Linear quadratic regulator (LQR) controller design for inverted pendulum* (Doctoral dissertation, Universiti Tun Hussein Malaysia).

[13] Agharkakli, A., Sabet, G.S. and Barouz, A., 2012. Simulation and analysis of passive and active suspension system using quarter car model for different road profile. *International Journal of Engineering Trends and Technology*, *3*(5), pp. 636-644.

[14] Ahmed, A.A., 2021. Quarter car model optimization of active suspension system using fuzzy PID and linear quadratic regulator controllers. *Global Journal of Engineering and Technology Advances*, *6*(03), pp. 088-097.

[15] Al-Mutar, W.H. and Abdalla, T.Y., 2015. Quarter car active suspension system control using fuzzy controller tuned by pso. *International journal of computer applications*, *127*(2), pp. 38-43.

[16] Ghazaly, N.M., Ahmed, A.E.N.S., Ali, A.S. and Abd El-Jaber, G.T., 2016. H∞ Control of Active Suspension System for a Quarter Car Model. *International Journal of Vehicle Structures & Systems (IJVSS)*, *8*(1), pp. 35-40.

[17] Shi, Y. and Eberhart, R., 1998, May. A modified particle swarm optimizer. In *1998 IEEE international conference on evolutionary computation proceedings. IEEE world congress on computational intelligence (Cat. No. 98TH8360)* (pp. 69-73). IEEE.

[18] Arumugam, M.S. and Rao, M.V.C., 2006. On the performance of the particle swarm optimization algorithm with various inertia weight variants for computing optimal control of a class of hybrid systems. *Discrete Dynamics in Nature and Society*, *2006*, pp. 1-17.

[19] Nurhadi, H., 2010. Study on Control of Bus Suspension System. Seminar Nasional Tahunan Teknik Mesin, *Department of Mechanical Engineering, Institut Teknologi Sepuluh Nopember (ITS)*, pp. 229-234.

SciEn
Journal of Engineering Advancements Vol. 04(01) 2023, pp 19-24 https://doi.org/10.38032/jea.2023.01.004

Development and Performance Evaluation of a Fixed Batch-type Pyrolysis Reactor for Bio-oil Production from Plastic Wastes

Taye Stephen Mogaji, Anthony Omoaka, and Olagoke Z. Ayodeji*

Department of Mechanical Engineering, School of Engineering and Engineering Technology, Federal University of Technology, P.M.B.704, Akure, Ondo State, Nigeria

Received: January 12, 2023, Revised: March 16, 2023, Accepted: March 18, 2023, Available Online: March 22, 2023

ABSTRACT

A fixed bed batch-type bioreactor for pyrolyzing used or discarded plastic wastes was developed and its performance was evaluated. This research explored the option of converting the high-density polyethylene (HDPE) category of plastic wastes into useful bio-oil in the developed pyrolysis fixed-bed batch reactor. The developed 5 kg batch-type pyrolysis system powered by liquified petroleum gas (LPG) was designed and simulated with SolidWorks computer software to confirm its functionality, fabricated with locally sourced materials, and evaluated with HDPE plastic wastes sorted from dumpsites within the Akure metropolis. The developed reactor evaluation result justified that the pyrolysis reactor has the potential to produce 1.4575 kg of bio-oil per kilogram of liquefied petroleum gas (LPG) consumed. The pyrolytic oil obtained at pyrolysis temperature between 280°C -520°C in this work was thereafter assayed for its composition and fuel properties analyses. The results of the characterization indicated that the pyrolysis of plastic HDPE wastes is a good source of alternative fuel as it shows proximity to the physiochemical characteristics of conventional diesel.

Keywords: Batch-type Pyrolysis System, HDPE Plastic Wastes, Bio-oil, Fuel Properties Analyses.

1 Introduction

Plastic waste generation has continued to increase in Nigeria over the last decade due to the growing population, rapid urbanization, and the increasing demand for sophisticatedly packaged fast-moving consumer goods (FMCG). Plastic has the advantages of easily forming, low cost, non-corrosive, durability, and lightweight, which had made embraced by most industries, including pharmaceutical and cosmetic industries, for packaging their products, which eventually leads to more plastic waste generation[1].

Plastic wastes have outgrown other most man-made materials, as they constitute about 12 % of the total municipal solid waste (MSW) all over the world [2]. Some of these plastic wastes find their way into water bodies through canals causing water pollution, aiding the breeding of mosquitoes, and channel blockage, which eventually leads to flooding.

As pointed out in the study of [3] some of the methods currently in use to control the menaces of plastic waste in the environment are recycling, landfilling, and incineration. The author reported that the landfilling method is not a sustainable option because it requires a large area and it can cause carbon sink which could lead to the leakage of a potential hazard to soil and water bodies, thereby endangering aquatic lives. The use of incinerator generates carbon monoxide, syngas, and other pollutants in the environment, which can affect human and contributes to the greenhouse effects. Reports from the open literature [4], [5], [6], [7], [8] have also pointed out that the oil crisis and environmental concern on the release of greenhouse gas (GHG) emissions from fossil fuel burning coupled with the fact that the magnitude of plastics production also brings with it, a global concern in related problems, including environmental pollution, unsustainable production, and poor recycling mechanisms as pointed out by Zhou *et al.* [9]. Hence there is a need to convert plastic waste into fuel which will reduce our dependency on fossil fuels and also reduce the hazards caused due to plastic waste. As we know that both Plastics and Petroleum derived fuels are Hydrocarbons that contain the elements of Carbon and Hydrogen. The pyrolysis process becomes an option of waste-to-energy technology to deliver biofuel to replace fossil fuels. According to Sharuddin [10], pyrolysis of plastic wastes has emerged as a promising chemical recycling method; it is capable of decomposing the plastic polymers into lower-molecular-weight products such as fuels and petrochemical feedstocks, to be used for energy or material recovery. More so, controlling the menaces of plastic waste in the environment by applying the Pyrolysis process is advantageous since it will give room for pre-treatment of the waste material in the area of handling unsorted and dirty plastic. The pyrolysis process is also of no toxic emission to the environment, unlike other commonly used disposal methods of waste plastics such as ocean dumping, sanitary landfill incineration, open dumping, and recycling. This method has been widely used to convert several MSW into useful oil by various researchers.

Mogaji *et al.* [7] worked on the production of bio-oil from the pyrolysis of sugarcane bagasse waste using a 3 kg capacity fixed-bed reactor with a maximum temperature of 500 ˚C. The chemical properties of the liquid produced (bio-oil) were analyzed and compared with the literature values of bio-oil obtained from other wastes. According to the research, the heating value of the bio-oil obtained from the pyrolysis of sugarcane bagasse is 17.33MJ/kg with a negligible amount of nitrogen (0.88 %) and sulfur (0.01 %). The report concluded that bio-oil produced from the pyrolysis of sugarcane waste has a negligible effect on the environment and it is suitable for running such equipment as boilers, reactors, etc. even without any further treatment. Wen *et al* [11] investigated the pyrolysis of corn Stover for bio-oil production using a fluidized bed reactor at a

*Corresponding Author Email Address: mogajits@gmail.com

temperature between 450 - 525 ˚C and the produced bio-oil was analyzed to determine its chemical properties (pH, kinetic viscosity, and calorific values) which were put at 3.99, 5.9 and 8.25 MJ/kg respectively. Gaurav *et al.* [12] researched the conversion of Low-density polyethylene (LDPE) plastic waste into bio-fuel by thermal degradation in a batch reactor and the output was fractionated in a distillation furnace. They submitted that LPDE yields 90 % bio-fuel, 6 wt% gases, and 4 wt% ash when subjected to pyrolysis. The high bio-oil yield of 87.97 wt%, 5.81 wt% gases, 6.22 wt% ash content was also established by Olufemi and Olagboye [13] while 89.5 wt% bio-oil, 10 wt% gases 0.5wt% ash by Sharuddin *et al*. [14]. One can conveniently say that LDPE has high vitality matter and good potential for an alternative source of biofuel. Onwudili *et al*. [15] investigated the pyrolysis of polystyrene (PS) in a batch pressurized autoclave reactor at 300–500˚C temperature range; the oil yield was 97.0wt%, 2.5wt% gas at an optimum temperature of 425˚C. The authors based on their findings concluded that PS can also be used in the production of biofuel.

However, many researches and findings have been made on some of the biodegradable and non-biodegradable waste as alternative sources of bio-fuel using pyrolysis process with no toxic emission to the environment, unlike other commonly used disposal methods of waste plastics such as ocean dumping, sanitary landfill incineration, open dumping, and recycling. Therefore, in order to gain more insight into one of the promising means of converting waste-to-energy technology to deliver bio-fuel to replace fossil fuel consider pyrolysis of HDEP plastic wastes. Research on the development of a 5.0 Kg batch-type bioreactor for pyrolyzing used or discarded plastic waste HPDE type was conducted and its performance was evaluated in this work.

2 Materials and Method

The materials entailed those used for developing the system, called fabrication materials, and for evaluating its performance, called feedstock, alongside the attached instrumentations. The fabrication materials whose properties and parameters, used equations and engineering standards as detailed in Table 1 were obtained from Alaaba and Owode-Onirin Markets in Lagos State and King Market in Akure. The feedstock, HDPE, was obtained from dumpsites within Akure Metropolis.

2.1 Design Analysis

The following design criteria were taken into consideration in this study**:**

i. Thermal decomposition of plastics operation takes about 3hrs between 500-550˚C [8], Hence 550˚C (T_1) is chosen as design temperature
ii. ambient temperature in Akure is 32˚C (T_2).
iii. The height of the reactor is 400 mm
iv. The operating pressure (p) within the reactor is 150000 N/m^2,
v. The factor of safety (F_s) is 4;
vi. The density of HDPE (ρ) is 959kg/m^3 [9],
vii. The efficiency of the welded joints (η) is 70 %
viii. The thermal conductivity of Ceramic wool insulator ($k_{ceramic\ wool}$) is 0.025W/m˚K;
ix. The thermal conductivity of mild steel (k_{ms}) is 43W/m˚K;
x. The maximum operating temperature of the reactor (T_{max}).is 800˚C

2.1.1 Reactor Shape Selection and Size Determination

The shape of the reactor was made cylindrical for design simplicity and ease of fabrication. The reactor, a batch-type, has a top cover for recharging feedstock and offloading residue respectively as it was designed to remain closed during operation. The volume of plastic waste to be charged into it per batch was determined using Eq. (1):

$$\rho = \frac{m}{V} \tag{1}$$

and the size of the reactor that could contain the estimated volume was obtained using Eq. (2):

$$V = h\pi r^2 \tag{2}$$

While considering the void factor to compensate for the void between a piece of feedstock, the actual radius (r_d) of the cylindrical reactor was determined using Eq. (3):

$$r_d = 4xr \tag{3}$$

The thickness of the reactor wall was determined by Eq. (4) as given by [16].

$$t = F_s \frac{p \times D}{2\,\sigma\,\eta} \tag{4}$$

where ρ is the density of HDPE (with the value of 959 kg/m^3, r, and h are the radius and h height of the cylinder, p is pressure in the reactor ($150000\mathrm{N/m^2}$). By substituting these values in Eq. (4), the dimensions of the reactor and its thickness are obtained as 504 mmØ and 4 mm respectively.

The flange (diameters d and D_o, thickness, t_f, width, B) of the reactor and bolt size (d), including the quantity required (n), were determined using Eq. (5) – (10) as follows:

$$d = 0.75t + 10mm \tag{5}$$

$$n = 0.0275D + 1.6 \tag{6}$$

$$t_f = 1.5t + 3mm \tag{7}$$

$$B = 2.3d \tag{8}$$

$$D_o = D + 2t + 2B \tag{9}$$

$$D_p = D + 2t + 2d + 12 \tag{10}$$

When values are substituted, the diameters (d, D_o) are 504 mm and 572 mm, with a width (B) of 30 mm to be fastened 16 pieces of M13 X40 bolts to the top of the reactor at pitch circle diameter (D_p) of 550 mm.

2.1.2 System Energy Requirement and Properties of Heating Element

The total energy (Q_T) and the total power (Q_P) required in the system, which connotes the heat energy needed to heat the feedstock through the various phases of depolymerization till complete pyrolysis, can be obtained using Eq. (11) and Eq. (12) as described by [17], [18].

$$Q_T = mc_p(Tm - T2) + ml_f + mc_p(T3 - T2) + mh_p \tag{11}$$

and

$$Q_P = Q_T + (Q_T \times \eta) \tag{12}$$

The length of the wire (L), number of coils (N_c) required for each coil of the heating element and their resistance per meter (A) was determined using Eq. (13) – (15), as described by [19].

$$x = \frac{l \times d \times 1000}{\pi \times (D + d)} \tag{13}$$

$$N_c = \frac{\pi \times D_R}{6.1} \times L \tag{14}$$

$$A = \frac{R}{N_c} \tag{15}$$

where: D_R is the reactor pot diameter, R is the resistance; when values were substituted, the electrical power required for a period of 3.0 hrs is 2.015 kW, and for NiCr 80:20 heating element at 20°C (R) whose temperature resistant factor (F) at 1000 °C is 1.062, the length and resistance per meter and of the heating element are 1.5 m and 0.45Ω/m respectively.

2.1.3 Determination of the System Insulation Thickness

Due to the high heat evolved in the reactor with the temperature of 800˚C, Ceramic wool was selected (T_{max}), the thickness of the insulator (t_{ins}) required resistance were determined using Eq. (16)-(17), according to [20].

$$Q = \frac{2\,\pi\, h\,(\Delta T)}{\frac{ln\left(\frac{r_2}{r_1}\right)}{K_{ms}} + \frac{ln\left(\frac{r_3}{r_2}\right)}{k_{ceramic}}} \tag{16}$$

$$t_{ins} = F.S\,(r_3 - r_2) \tag{17}$$

Where: r_1 and r_2 are the pot's internal and external pot radii, r_3 is the external radius of the insulator,

2.1.4 Design of Condenser

The plastic vaporization production rate ((PVPR) was determined using Eq. (18);

$$PVPR = \frac{Heat\ transfer\ rate}{latent\ heat\ of\ vapourization} \tag{18}$$

Based on the principle of energy balance that the heat lost by the plastic vapor oil is equal to the heat gained by the cooling water, and heat dissipated to the condenser to cause phase changing of the vapour (condensate), the production rate of the oil, cooling water demand and geometric properties of the heat exchanger (number of tubes N_t) with its overall heat transfer coefficient (U_E) were determined using Eq. (19)- (20), according to [21];

$$Q_T = \dot{m}_{oil} c_p \Delta T = \dot{m}_w c_w \Delta = U\ A\ \ \Delta T_m \tag{19}$$

$$N_t = \frac{A}{\pi D_i L} \tag{20}$$

where: c_p and c_w are the specific heat capacity of the oil and cooling water, ΔT is the logarithm temperature difference (LMTD), A is the heat transfer surface area of the condenser. When values are substituted, the mass flow of water required ($\dot{m}_w$) is 0.066 kg/s (237.6 kg/h), the mass of oil ($\dot{m}_{oil}$) produced is 0.0071kg/s (25.56 kg/h), whilst the computed A and N_t of the condenser are: 0.394m^2 and 9.57 nos, but 10 nos were adopted.

2.2 Validation of the Estimated Design Data Utilized for Developing the Reactor and Condenser

In order to achieve the designed and desired reactor temperature, the heat energy within the system must be preserved; hence, the reactor composite wall was subjected to simulation with SolidWorks computer software. The inner, and outer layers and the insulator that made up the proposed reactor unit wall were assigned, carbon steel, and ceramic wool, Afterward, the designed thermal loads were applied. Fig. 1 presents the results of the thermal analysis. The simulated results revealed that a maximum temperature between 524 and 568°C could be attained; more so, it also indicated that a section of the wall towards the outer surface still maintains the originally assigned temperature of 32°C while a section of the wall from the inner surface maintains the maximum temperature of 568°C. Thus, the findings of the simulation depicted that the reactor is suitable enough to pyrolyze plastic waste at the required burning temperature as the design parameters (temperatures) considered for the reactor lie within the range.

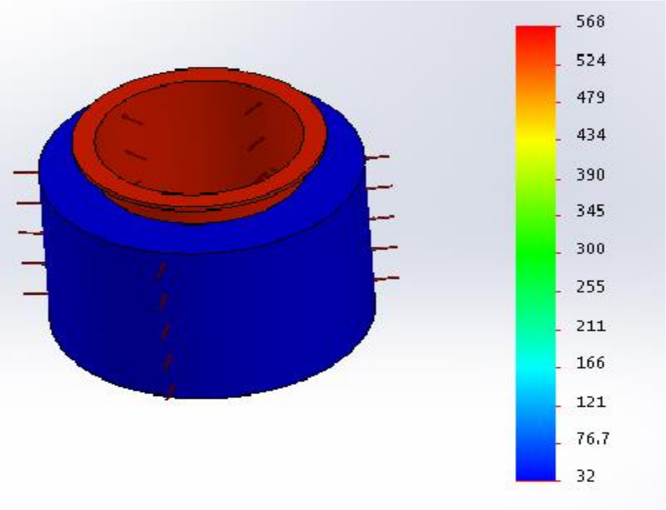

Fig. 1 Simulation Report of the Reactor

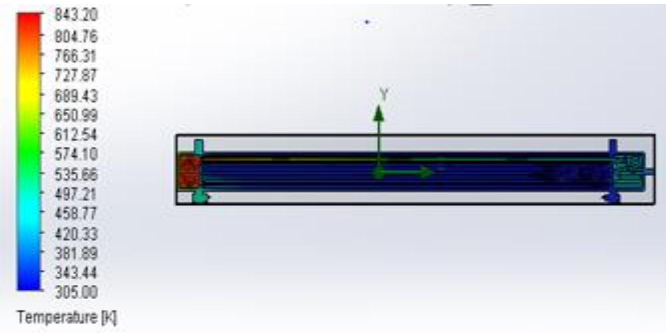

Fig. 2 Condenser Simulation Chart

More so, as the heat energy of the hydrocarbon vapour entry from the cracking unit must be given off, the condenser was subjected to SolidWorks flow simulation by assigning the calculated fluids flow rate, boundary conditions, fluid types, environmental pressure, mesh goals, etc., Fig. 2 presents the simulation output result condenser unit of the system. From the simulation result an average fluid temperature of 332K (~ 59°C) could be attained in the condenser component; a value reasonably closer to the proposed fluid temperature (60°C) selected in the course of designing the condensing unit. Also, it can be seen from Fig. 2 that the proposed entry water to the condensing unit section of the system still maintains the originally assigned temperature of 305 K (~32°C) Thus, the simulation output indicates that the condenser is capable enough to condense the expected heat-laden-vapour generated that exits from the pyrolysis of the feedstock.

2.3 Materials Gathering and Machine Fabrication

The materials comprise the fabrication and machine performance evaluation material (termed feedstock). The fabrication materials, which are mild steel, aluminum, copper, and ceramic wool, and the instrumentations were procured from Arakale Market in Akure, Ondo State, and Alaba Market in Lagos. Fig. 3 presents the isometric view of the developed plastic pyrolyzer and Table 1 shows the specifications of the developed pyrolysis system.

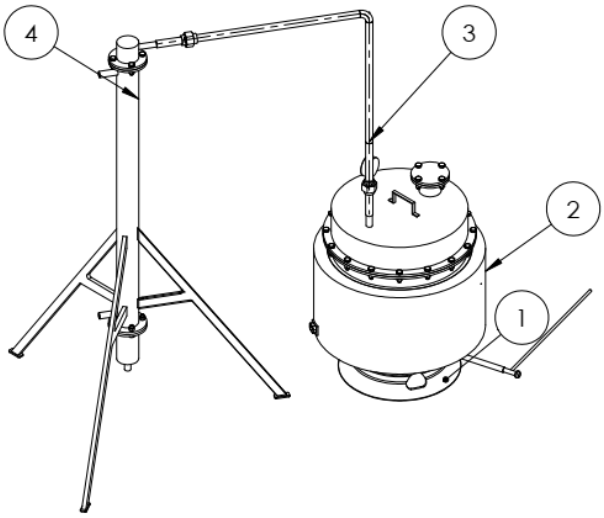

Fig. 3 Isometric View of the Developed Plastic Pyrolyzer

Table 1 Specifications of the developed plastic pyrolyzer

S/N	Name	Description	Quantity
1	Gas Burner	1500 btu/hr. LPG Burner	1
2	Reactor	-	1
3	Pipe	24 mm mild steel pipe	2
4	Condenser	Single-pass shell=tube condenser	1

Waste plastic, the feedstock, was obtained from waste sites located within Akure Metropolis. The feedstock was cleaned to remove impurities. it was then cut into the size of 50 mm by 50 mm with the aid of a hacksaw and Grinding machine (Model: Bosch) to facilitate ease loading into the reactor chamber.

The machine was fabricated and subjected to performance evaluation at the Central Workshop of the Department of Mechanical Engineering of the Federal University of Technology, Akure. Also, all other consumables (such as water,) were obtained from the premises of the University.

2.4 Experimental Setup and Performance Test

Performance evaluation of the developed pyrolysis plant (Test rig) was done using samples of the High-Density Polyethylene (HDPE) type of plastic waste, the selected feedstock, sourced within the Akure metropolis. Prior to the commencement of the evaluation, the Test rig condenser was connected to the water source and filled up. Afterward, a measured quantity (5 kg) of the feedstock (HDPE) measured with a spring dial mechanical weighing scale was charged into the reactor. The reactor lid (cover) was closed and fastened in position with 6 pieces of M12 bolts to prevent air ingress. The reactor burner was then ignited to raise the test rig to the designed pyrolysis temperature (550˚C) preset using the attached automatic temperature controller. The pyrolysis process was allowed to continue until no fraction was obtained anymore. The temperature at which the first drop of condensate dropped into the beaker as well as the last drop, including their associated time, was noted with the attached temperature measuring instrument and stopwatch. Also, the temperatures of the cooling water exiting the condenser were recorded at an interval of 30 minutes. At end of the last drop, the Test rig was disengaged from the power source and allowed to cool. Afterward, the reactor lid was again removed, and the remaining fraction, of biochar, left in the reactor was removed (and weighed or its mass recorded). Fig. 4 presents the experimental setup, bottled bio-oil obtained in this study, and the flame test bottle.

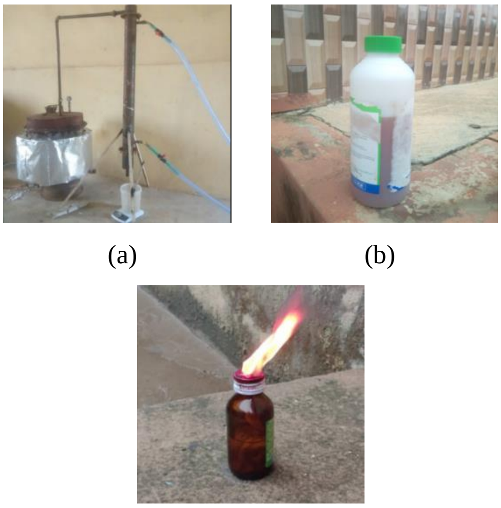

(a) (b)

(c)

Fig. 4 (a) Experimental setup, (b) Bio-oil, and (c) Flame Test

2.4.1 Transesterification Process Carried Out in this Study

Transesterification was performed with a 500 mL tabletop-mounted biodiesel processor. A unit mass of 300 g of sodium methoxide was measured and mixed with the measured quantity of the extracted oil obtaining a molar ratio of 6:1. The mixture formed was then raised in temperature to 60 °C by heating and stirred at 450 rpm for 2 hours. Afterward, the mixture was poured into a separatory funnel and left for 8 hours to allow the reaction to reach equilibrium and facilitate the biodiesel with glycerol to separate into two distinct layers. The glycerol, at the bottom, was drained off by gravity and the excess methanol in the biodiesel was removed using a reduced pressure (20 mbar, 30 °C) rotary evaporation. The crude biodiesel was washed with distilled water until a neutral pH value was obtained and, then, dried by passing over magnesium sulfate.

2.4.2 Determination of the Mass of LPG Used

In order to estimate the quantity of fuel, LPG used to achieve the pyrolysis in this study, the mass of the charged LPG gas cylinder before experimentation was measured with a spring balance and recorded (as m_1 value of 7.0 kg). The final mass of the cylinder at the end of the process was then noted and recorded (as m_2). The fuel consumption per batch (m_{fc}) was obtained using Eq. (21):

$$\mathrm{m_{fc}} = \mathrm{m_1} - \mathrm{m_2} \tag{21}$$

After experimentation, the final mass of the charged LPG gas was found to be 6.2 kg; this shows that 0.8 kg of LPG gas was used for firing the reactor during the pyrolysis process

2.5.3. Bio-oil productivity per fuel consumption (ϕ_p)

The Bio-oil productivity per fuel consumption, defined as the ratio of the bio-oil produced ($\mathrm{m_{bf}}$) to the mass of fuel consumed ($\mathrm{m_{fc}}$) to achieve the pyrolysis process can be determined using Eq. (22):

$$\varphi_{\mathrm{p}} = \frac{\mathrm{m_{bf}}}{\mathrm{m_{fc}}} \tag{22}$$

It was observed that when the bio-oil produced was weighed with a digital mass balance, the mass of bio-oil produced per the feedstock charged used in this work is obtained as 1166 g. Hence, the bio-oil productivity per fuel consumption using Eq. (22) is calculated as 1.4575 kg/kg.

3 Results and Discussion

Samples of the bio-oil obtained, grouped as A, B, and C were subjected to physicochemical analyses at Chemical Laboratories of the Federal Institute of Industrial Research Oshodi (FIIRO), Lagos State, and the Chemistry Department at Federal University of Technology Akure (FUTA), Ondo State; according to the procedures specified by American Oil Chemists' Society (AOCS, 1990) and American Society for Testing and Materials (ASTM) methods considered for characterization of bio-oil and biodiesel

Table 2 presents details of the characteristics of the bio-oil obtained from the pyrolysis of the HDPE plastic waste, using the developed Test rig in this study.

Table 2 Characteristics of Bio-Oil obtained from HDPE Plastic Wastes

S/N	Property	Sample A	(Unrefined oil) Sample B	(Refined oil) Sample C	Tested Method
1	Acid value	0.444	0.726	0.450	
2	Saponification value	89.047	98.414	88.022	
3	Iodine value	7.016	8.500	6.108	
4	Specific gravity	0.818	0.785	0.778	
5	Kinematic viscosity (m^2/s)	10.307	0.953	0.820	ASTM D 445
6	Flashpoint (˚C)	145.000	39.400	32.785	ASTM D 93
7	Volatile matter (%)	1.539	97.400	99.710	
9	Pour point (˚C)	22.000	-32.000	-29.000	ASTM D 97
10	Density (kg/m^3)	962.000	785.000	778.000	ASTM D1298
11	Heating value (kJ/g) 42 – 46	-	39.525	41.231	ASTM D240

With reference to Eq. (21) and Eq. (22) respectively, it was computed that: (i) 0.8 kg of LPG gas was used to fire the test rig while pyrolyzing 5.0 kg HDPE plastic (or 0.16 kg of LPG gas would pyrolyze 1.0 kg of feedstock); (ii) for 5.0 kg HDPE (feedstock) charged for pyrolysis process, 1.166 kg of bio-oil is produced. Similarly, 1.0 kg of feedstock would yield 233.2 g of bio-oil, and (iii) the bio-oil productivity per fuel consumption given as (φ_p) in Eq. (22) is calculated as 1.4575. It should be highlighted that since the φ_p>1, it can be inferred that pyrolysis of considered HDPE plastic wastes is a good alternative source for converting waste to biofuel production

From Table 2, Sample A refers to the denser fluid ratio of pyrolytic oil obtained, it accounts for about 5.4 % of the total condensate collected. Sample B is the remaining portion of the total condensate collected (94.6 %); it is the unrefined bio-oil yield. Sample C is the esterified refined bio-oil yield as aforementioned above. The 94.6 % bio-oil yield depicts the ability of HDPE wastes to yield more bio-oil compared to those reported in the studies of Akinola *et al.* [22], Mogaji *et al* [7], Babajo *et al* [23], and Khuenkaeo *et al* [24]).

It is also found that the heating values of samples shown in Table 2 are almost close to the heating values of the available various fuels, viz: diesel (42 – 46 MJ/kg); crude oil (42 – 47 MJ/kg); LPG (46 – 51 MJ/kg), and natural gas (42 – 55 MJ/kg) and greater than that of solid fuel, like wood (with a value of 17 MJ/kg) and within the range of that of vegetable oil (31 – 48 MJ/kg), this outcome shows that pyrolysis of discarded plastic wastes is a good potential alternative biofuel production source.

The flashpoint of 145 ˚C for sample A indicates that it is not a combustible substance compared to 39.4 ˚C and 32.785 ˚C flashpoint values attained for samples B and C respectively. The achieved flashpoint values for samples B and C (which indicate the lowest temperatures at which its vapour will ignite with a low flame) revealed that they are highly combustible liquid substances as buttressed by the flame test shown in Plate 3. The high value of the flashpoint of sample A, which is higher than that specified for diesel, depicts that it is a safer fuel than diesel; this result aligned with the findings of Bello *et al.*, [25]. This outcome shows that bio-oil from the pyrolysis of discarded plastic is a good potential energy source as it has fuel properties similar to that of petroleum fuels.

4 Conclusion

A 5.0 kg batch-type bioreactor for pyrolyzing used or discarded plastic waste has been developed and its performance was evaluated in this study. The evaluation of HDPE waste through Pyrolysis and the creation of a new value for this type of waste was the focus of this study. The pyrolytic oil obtained from the developed system at temperatures between 280ºC -520ºC was assayed for composition and fuel properties. The performance result revealed that the developed pyrolysis reactor in this study has the potential to produce 1.4575 kg of bio-oil per kilogram of liquified petroleum gas (LPG) consumed. These results justified that the burning of fossil fuel (LPG) to obtain bio-oil from the HPDE plastic waste pyrolyzed in this work is cost-effective and beneficial to achieve alternative biofuel production. The reduced fuel densities of 785 and 778) kg/m^3 for Samples B and C respectively revealed that the alternative biofuel produced in this study would be more environmentally friendly as a considerable reduction in the concentrations of Carbon IV Oxide (CO_2), unburnt hydrocarbon (HC) and soot emitted when used in light duty engines. The observed flame result from obtained pyrolytic oil in this study confirmed that they are combustible liquid substances. It is also found that the heating value 41.231 kJ/g obtained for the esterified Sample C bio-oil in this work is almost a close match with the heating value (42-46) kJ/g of the conventional diesel fuels. Thus, the research yields diesel-like fuel whose properties are similar to that of conventional diesel. However, further post-processing steps are imperative to upgrade the fraction to meet up with regulation standards and specifications.

Acknowledgment

The authors would like to acknowledge the assistance of the Refrigeration and Air Conditioning Unit of the Department of Mechanical Engineering, the Federal University of Technology Akure in supplying relevant information used in the present study.

Conflict of Interest

The authors declared that there is no conflict of interest in the article.

References

[1] Aziz, M.A., Al-Khulaidi, R.A., Rashid, M.M., Islam, M.R. and Rashid, M.A.N., 2017, March. Design and fabrication of a fixed-bed batch type pyrolysis reactor for pilot scale pyrolytic oil production in Bangladesh. In *IOP Conference Series: Materials Science and Engineering* (Vol. 184, No. 1, p. 012056). IOP Publishing.

[2] Geyer, R., Jambeck, J.R. and Law, K.L., 2017. Production, use, and fate of all plastics ever made. *Science advances*, *3*(7), p.e1700782.

[3] Chanashetty, V.B. and Patil, B.M., 2015. Fuel from plastic waste. *International Journal on Emerging Technologies*, *6*(2), p.121.

[4] Abnisa, F., Daud, W.W. and Sahu, J.N., 2011. Optimization and characterization studies on bio-oil production from palm shell by pyrolysis using response surface methodology. *Biomass and bioenergy*, *35*(8), pp.3604-3616..

[5] Goyal, H.B., Seal, D. and Saxena, R.C., 2008. Bio-fuels from thermochemical conversion of renewable resources: a review. *Renewable and sustainable energy reviews*, *12*(2), pp.504-517.

[6] Titiladunayo I.F., 2002. Biomass Energy Conversion and the Impact of Bioenergy Utilization on the Environment. *Nigerian Journal of Forestry*, *32*, pp.42-49.

[7] Mogaji, T. S. Akinsade, A., Akintunde, M. A., 2019**.** Pyrolysis of Sugarcane Bagasse for Bio-Oil Production. *Journal of Engineering and Engineering Technology, 13*(2**)**, pp.150-157.

[8] Mogaji, T.S., Moses, E.O., Idowu, E.T. and Jen, T.C., 2020. Thermal Degradation Conditions Effects on Selected Biomass Wastes and Characterization of Their Produced Biochar.

[9] Zhou, N., Dai, L., Lv, Y., Li, H., Deng, W., Guo, F., Chen, P., Lei, H. and Ruan, R., 2021. Catalytic pyrolysis of plastic wastes in a continuous microwave assisted pyrolysis system for fuel production. *Chemical Engineering Journal*, *418*, p.129412.

[10] Sharuddin, S.D.A., Abnisa, F., Daud, W.M.A.W. and Aroua, M.K., 2016. A review on pyrolysis of plastic wastes. *Energy conversion and management*, *115*, pp.308-326.

[11] Wen, Y., Peng, F. and Weiming, Y., 2017. Catalytic fast pyrolysis of corn stover in a fluidized bed heated by hot flue gas: Physicochemical properties of bio-oil and its application. *International Journal of Agricultural and Biological Engineering, 10*(5), pp.226-233.

[12] Gaurav, M.M., Arunkumar, K.N. and Lingegowda, N.S., 2014. Conversion of LDPE plastic waste into liquid fuel by thermal degradation. *International Journal of Mechanical and Production Engineering*, *2*(4), pp.104-107.

[13] Olufemi, A.S. and Olagboye, S., 2017. Thermal conversion of waste plastics into fuel oil. *Int. j. petrochem. sci. eng*, *2*(8), pp.252-257.

[14] Sharuddin, S.D.A., Abnisa, F., Daud, W.M.A.W. and Aroua, M.K., 2018, March. Pyrolysis of plastic waste for liquid fuel production as prospective energy resource. In *IOP Conference Series: Materials Science and Engineering* (Vol. 334, p. 012001). IOP Publishing.

[15] Onwudili, J.A., Insura, N. and Williams, P.T., 2009. Composition of products from the pyrolysis of polyethylene and polystyrene in a closed batch reactor: Effects of temperature and residence time. *Journal of Analytical and Applied Pyrolysis*, *86*(2), pp.293-303.

[16] Khurmi, R.S. and Gupta, J.K. (2015): “A Textbook on Refrigeration and Air Conditioning.” Eurasia Publication House (P) Ltd, New Delhi. Page 360-368.

[17] Khedri, S. and Elyasi, S., 2018. Determination of the heat of pyrolysis of HDPE via isothermal differential scanning calorimetry: A new approach for solid state reactions. *Journal of Thermal Analysis and Calorimetry*, *131*, pp.1509-1515.

[18] Ineos, 2019. Typical Engineering Properties of High-Density Polyethelene, *Ineos olefins and polymers*, USA: www.ineos-op.com accessed 11/12/2019.

[19] Alloy Wire International, 2019: https://www.alloywire.com/downloads/ accessed 15/10/2019.

[20] Rajput K. R., 2011. A Textbook of Heat and Mass Transfer, Revised Edition, Chand and Company Ltd. publication, 7361, Ram Nagar, New Delhi, India, pp.80-95

[21] Serth, R.W., 2007. Process Heat Transfer Principles and Applications. Department of Chemical and Natural Gas Engineering, Texas A&M University-Kingsville, Kingsville, Texas, USA

[22] Akinola, A.O., Eiche, J.F., Owolabi, P.O. and Elegbeleye, A.P., 2018. Pyrolytic analysis of cocoa pod for biofuel production. *Nigerian Journal of Technology*, *37*(4), pp.1026-1031.

[23] Babajo, S.A., Enaburekhan, J.S. and Rufa’i, I.A., 2021. Design, fabrication and performance study of co-pyrolysis system for production of liquid fuel from jatropha cake with polystyrene waste. *Journal of Applied Sciences and Environmental Management*, *25*(3), pp.407-414.

[24] Khuenkaeo, N., Phromphithak, S., Onsree, T., Naqvi, S.R. and Tippayawong, N., 2021. Production and characterization of bio-oils from fast pyrolysis of tobacco processing wastes in an ablative reactor under vacuum. *PLoS One*, *16*(7), p.e0254485.

[25] Bello E. I; Ayodeji, O. Z; Ogunbayo, S. and Bello, K., 2019. Characterization and Glycerine Analysis of Mustard (Brassica juncea. L) Seed Oil and Biodiesel, *Journal of Advances in Biology and Biotechnology*, *22*(2), pp.1 – 8.

SciEn
Journal of Engineering Advancements Vol. 04(01) 2023, pp 25-34 https://doi.org/10.38032/jea.2023.01.005

Numerical Analysis on Cavitation-noise and Fluid-structure Interaction of AU-Outline GAWN Series and B-Series Marine Propellers

Md. Iftekharul Alam, Abidur Rahman Adib, Abdullah Al Rifat, Tafsirul Hassan, Md. Mizanur Rahman*

Department of Mechanical Engineering, Chittagong University of Engineering & Technology, Chattogram-4349, Bangladesh

Received: February 24, 2023, Revised: March 21, 2023, Accepted: March 23, 2023, Available Online: March 26, 2023

ABSTRACT

Cavitation and cavitation-induced noise are harmful to both marine propellers and marine wildlife. Thus, it is required to reduce cavitation in marine propellers by developing the best design marine propellers. Moreover, proper material should be selected during the construction of marine propellers to withstand high-pressure loads. This paper presents an evaluation of the hydrodynamic characteristics such as cavitation and cavitation-induced noise of AU-outline GAWN series and B-series marine propellers at 0˚, 5˚, 10˚, and 15˚ rake angles using Computational Fluid Dynamics (CFD) analysis. Moreover, the study aims to find out the optimized propeller material among Nickel-Aluminum-Bronze (NAB), S2 glass, Aluminum 6061, and carbon fiber reinforced plastic (CFRP) materials. It is concluded that the lowest cavitation noises are 153.3 dB and 153.1 dB at a 10° rake angle for AU-outline GAWN series and B-Series marine propellers respectively. S2 glass is observed to be the optimum material at low rake angles, while CFRP is the optimum material at high rake angles compared to all other potential materials for both AU-outline GAWN series and B-series propellers.

Keywords: Marine Propellers, AU-Outline GAWN Series, B-Series, Cavitation Noise, Rake Angle.

1 Introduction

Ships and marine vehicles are able to maneuver themselves in the water because of the propulsion forces they use. Marine propellers are rotating devices with several blades to produce linear thrust on the water to move the corresponding marine vehicles. For efficient propulsion, the proper design of marine propellers is required. Predicting and determining the propulsive efficiency of ship design at the pre-design stage is a need. The proper propeller blade design is a quite difficult task because it has to make sure the reduction of cavitation, noise, erosion, and increasing of its life while improving efficiency [1]. The process of designing a propeller is also limited by certain hydrodynamics factors, such as the Reynolds number and maximum diameter in the event of weight loading, among others [2]. Cavitation and cavitation-induced noises are also included as barriers in the case of proper designing of marine propellers. Conforming to Bernoulli's principle, cavitation is the formation of vapor bubbles in the water near a rotating propeller blade in areas of low pressure. There are several types of cavitation that occur in marine propellers such as bubble cavitation, sheet cavitation, cloud cavitation, tip and vortex cavitation, blade root cavitation, etc. [3]. There are two types of noise induced by the propeller, non-cavitating noise, and cavitation noise. Collapsing cavitation bubbles generate shock waves, which result in noise also known as cavitation noise. This is basically 'white noise' up to around 1 MHz in frequency. The amount of noise produced by a cavitating propeller is dependent on the kind of cavitation present at the time of operation [4]. The noise generated due to cavitation is more dangerous. The effect of marine propeller cavitation noise is higher than that of propeller non-cavitation noise [5]. Thus, the prediction and reduction of marine propeller cavitation noise is a must. Moreover, marine propellers must operate in saltwater, which is a corrosion-promoting environment. Thus, corrosion-resistant materials must be used in their production. Aluminum and stainless-steel alloys are the primary materials used in the manufacture of maritime propellers. Besides, there are also many other materials available to manufacture maritime propellers. The marine propeller designs must be such that those are with less cavitation and cavitation noise with higher pressure load sustaining. For designing and investigating marine propellers, there are different approaches such as numerical, analytical, experimental, etc. At present, numerical analysis of marine propellers such as computational fluid dynamics (CFD), structural analysis, etc. are becoming more popular besides experimental approaches. For example,Ősschers and Wijngaarden [6] conducted computational and experimental studies to predict the noise induced by cavitation. Three of the EU's SONIC project ship designs such as a cruise liner, a container vessel, and a catamaran designs were studied to observe how the noise from cavitation was predicted using computational and experimental techniques. It was found that the ETV-model provides acceptable agreement with the observed noise levels validated through full-scale trials on a cruise liner. The empirical model for sheet cavitation noise shows better results than the ETV model for a container vessel. The empirical result for a catamaran in MARIN's DWB showed significant variation that demands further investigation further. In overall, the prognostications of the ETV-model and the Brown-model belong to the range of observations. Bagheri et al. [7] carried a research work to analyze both cavitation and non-cavitating noise characteristics. Using the finite volume technique, they investigated the hydrodynamics and noise behavior of maritime propeller models (I and II) under a variety of operating circumstances. For the model I, it was observed that the cavitation fully occurred at J = 0.125 and the total SPL variations

*Corresponding Author Email Address: tafsir2086@gmail.com

Published by: SciEn Publishing Group

between cavitating and non-cavitating conditions fluctuated between 15-40 dB. These results also vary from 4-20 dB for J = 0.125 and 0.166. For model II, cavitation occurred at J = 0.32 and total SPLs was calculated at J = 0.8, 0.6, 0.4, and 0.32 also. Total SPLs under cavitating conditions for N = 1850 rpm and J = 0.32 were found to be higher than total SPLs under non-cavitating conditions for N = 800 rpm and J = 0.4. Numerical research was conducted by Usta et al. [8] on the prediction of performance, cavitation, and erosion features of the King's College-D (KCD)-193 model marine propeller under various flow conditions. They used an unstable Detached Eddy Simulation (DES) turbulence model in conjunction with the Computational Fluid Dynamics (CFD) program STAR-CCM+. Three different approaches were used to model cavitation erosion on the propeller blades, with pressure, saturation pressure, the volume fraction of vapor, the time derivative of pressure, and time derivative of the volume fraction of vapor on the propeller blades obtained from simulations as input variables. The authors presented a novel method for predicting the severity of cavitation erosion on the propeller blade. Yamatogi et al. [9] studied composite materials for marine propellers while they were trying to develop a composite material made up of marine propellers having ship energy conservation. They examined the cavitation erosion of different types of composite materials and revealed that fibre-reinforced plastics (FRPs) were not resistant to the erosion caused by cavitation to which the marine propeller was subjected throughout the research. However, it was concluded that the erosion resistance of aluminum bronze (NAB), which is often used for maritime propellers, was much higher than that of any other FRPs. The erosion resistance of GFRPs was lower than that of CFRPs where AFRPs showed the strongest erosion resistance among FRPs. On further investigation, it was concluded that there were fibre bundles with resin in CFRPs, while there were few fibre bundles in the case of GFRPs and the fibres of GFRPs were longer than those of CFRPs. While designing four-bladed marine propellers, the study focused on engines producing 85 bhp and ships traveling at 30 knots, which were both considered to be high-performed [10]. Static analysis was accomplished on an aluminum composite propeller that was made up of a mix of R Glass, S2 Glass, and CFRP (Carbon Fiber Reinforced Plastics). It was decided to use different sections for the single blade utilizing HYDRO PROCAD, and using section coordinate data, a 3D 4-blade propeller was modeled in CATIA V5R20 and analysis was conducted using ANSYS. Again, investigators utilized DTMB 4119 marine propeller model in a series of computational tests that evaluated the Blade Stress while conducting operations in open water [11]. The blade axial strain and the propeller flow field distribution also had their corresponding stress distribution investigated. The data gathered from ANSYS FLUENT simulations provided very precise and trustworthy hydrodynamic load calculation results for the propeller construction.

There have been huge research works to develop and improve the design of marine propellers. Many series and types of marine propellers have been developed till now. However, all these modern designs of marine propellers are still in their infancy. Marine propeller materials are needed to avoid and sustain cavitation-induced damages and noises. There are many different parameters such as variation in the blade section, rake and skew angle change, material change, etc. to reduce the cavitation and its induced noise. Cavitation, corrosion, impact loading, cavitation-induced noises, biological invasions, fractures, and fatigue are some of the problems that marine propellers still face while operating. Thus, the aim of this research is to predict and investigate the hydrodynamic characteristics, cavitation, and cavitation-induced noise within proper boundary conditions by varying the rake angles of AU-outline GAWN series and B-series marine propellers. Another aim of this study is to choose the best material among Aluminum 6061 alloy, Nickel-Aluminum-Bronze (NAB), S2 glass, and carbon fibre-reinforced plastic (CFRP) materials based on structural criteria. Both series of marine propellers with the variation of rake angles of 0°, 5°, 10°, and 15° respectively have been modeled in PropCad 2005 and SOLIDWORKS 2020. The CFD and one-way FSI simulations were done in ANSYS 19.2. Finally, the results of both CFD and static structural analysis are compared with published literature.

2 Materials and Method

Firstly, AU-outline GAWN series and B-series marine propellers of the same diameter with the variation of rake angles of 0°, 5°, 10°, and 15° respectively (total 8 marine propellers) are modeled and combined in both PropCad 2005 and SOLIDWORKS 2020. Then cavitation, hydrodynamics characteristics, and cavitation-induced sound pressure level (SPL) are investigated in ANSYS FLUENT. The pressure loads are imported in static structural analysis and one-way fluid-structure interaction (FSI) is used with the variation of four different materials such as Aluminium 6061 alloy, Nickel-Aluminium-Bronze (NAB), S2 Glass, and carbon fiber reinforced plastic (CFRP). After the completion of the simulations, a comparison among the obtained results is done to determine the intended outcome.

2.1 Propeller models

Both PropCad 2005 and SOLIDWORKS 2020 software have been used in designing both AU-outline GAWN series and B-series marine propellers. At first, marine propeller blades have been modeled in PropCad and hubs of marine propellers have been modeled in SOLIDWORKS later. Both series of marine propellers have the same diameter of 0.304 m and rake angles of 0°, 5°, 10°, and 15° respectively. The marine propeller design properties for both series are given in Table 1.

Table 1 Design properties of marine propellers (AU-outline GAWN and B-series) [12].

Parameter	Value
Marine propeller diameter	0.3048 m
Number of marine propeller blades	5
Skew angle	0°
Expended area ratio	0.725
Nominal pitch	0.36576 m
Rake angles	0°, 5°, 10°, and 15°

Those general parameters were the same in the design of both AU-outline GAWN series and B-series marine propellers. By changing the rake angles of 0°, 5°, 10°, and 15° respectively for both series AU-outline GAWN series and B-series, a total of 8 marine propellers have been modeled.

2.2 Mathematical Models

2.2.1 The Navier-Stokes Equation

ANSYS FLUENT is a robust and sophisticated CFD tool which is a finite volume method-based tool. The Navier-Stokes equation is the governing equation of the CFD analysis which is a partial differential equation that defines the flow characteristics of incompressible fluid as given below:

Continuity equation:

$$\frac{\partial \rho}{\partial t}+\frac{\partial(\rho u)}{\partial x}+\frac{\partial(\rho v)}{\partial y}+\frac{\partial(\rho w)}{\partial z}=0 \tag{1}$$

Conservation of momentum:
In x-direction:

$$\frac{\partial(\rho u)}{\partial t}+\frac{\partial(\rho u^2)}{\partial x}+\frac{\partial(\rho uv)}{\partial y}+\frac{\partial(\rho uw)}{\partial z}=-\frac{\partial p}{\partial x}+\frac{1}{\mathrm{Re}}\left(\frac{\partial\tau_{xx}}{\partial x}+\frac{\partial\tau_{xy}}{\partial y}+\frac{\partial\tau_{xz}}{\partial z}\right), \tag{2}$$

In y-direction:

$$\frac{\partial(\rho v)}{\partial t}+\frac{\partial(\rho uv)}{\partial x}+\frac{\partial(\rho v^2)}{\partial y}+\frac{\partial(\rho vw)}{\partial z}=-\frac{\partial p}{\partial y}+\frac{1}{\mathrm{Re}}\left(\frac{\partial\tau_{xy}}{\partial x}+\frac{\partial\tau_{yy}}{\partial y}+\frac{\partial\tau_{yz}}{\partial z}\right), \text{ and} \tag{3}$$

In z-direction:

$$\frac{\partial(\rho w)}{\partial t}+\frac{\partial(\rho uw)}{\partial x}+\frac{\partial(\rho vw)}{\partial y}+\frac{\partial(\rho w^2)}{\partial z}=-\frac{\partial p}{\partial z}+\frac{1}{\mathrm{Re}}\left(\frac{\partial\tau_{xz}}{\partial x}+\frac{\partial\tau_{yz}}{\partial y}+\frac{\partial\tau_{zz}}{\partial z}\right). \tag{4}$$

2.2.2 2.2.2 The SST k-ω Turbulence Model

The SST k-ω turbulence model is a two-equation eddy-viscosity model which was modified by Menter [13] from standard k-ω model [14]. The SST k-ω model generates a little too much turbulence in regions with substantial normal strain, such as stagnation regions and regions with rapid acceleration. In contrast to a typical k-ϵ model, this tendency is significantly less pronounced. Due to adverse pressure gradient and strong curvature regions, the K-ω SST model has been selected in this study [15].

Kinematic eddy viscosity,

$$v_T=\frac{a_1 k}{max(a_1\omega, SF_2)} \tag{5}$$

Turbulence kinetic energy,

$$\frac{\partial k}{\partial t}+U_j\frac{\partial k}{\partial x_j}=P_k-\beta^* k\omega+\frac{\partial}{\partial x_j}\left[(\nu+\sigma_k\nu_T)\frac{\partial k}{\partial x_j}\right] \tag{6}$$

Specific dissipation rate,

$$\frac{\partial\omega}{\partial t}+U_j\frac{\partial\omega}{\partial x_j}=\alpha S^2-\beta\omega^2+\frac{\partial}{\partial x_j}\left[(\nu+\sigma_\omega\nu_T)\frac{\partial\omega}{\partial x_j}\right]+2(1-F_1)\sigma_{\omega 2}\frac{1}{\omega}\frac{\partial k}{\partial x_i}\frac{\partial\omega}{\partial x_i} \tag{7}$$

where,

$$F_2=tan\,h\left[\left[max\left(\frac{2\sqrt{k}}{\beta^*\omega y},\frac{500\nu}{y^2\omega}\right)\right]^2\right],$$

$$P_k=min\left(\tau_{ij}\frac{\partial U_i}{\partial x_j},10\beta^* k\omega\right),$$

$$F_1=tanh\left\{\left\{min\left[max\left(\frac{\sqrt{k}}{\beta^*\omega y},\frac{500\nu}{y^2\omega}\right),\frac{4\sigma_{\omega 2}k}{CD_{k\omega}y^2}\right]\right\}^4\right\}$$

$$CD_{k\omega}=max\left(2\rho\sigma_{\omega 2}\frac{1}{\omega}\frac{\partial k}{\partial x_i}\frac{\partial\omega}{\partial x_i},10^{-10}\right),$$

$$\phi=\phi_1F_1+\phi_2(1-F_1),\alpha_1=\frac{5}{9},\quad \alpha_2=0.44,$$

$$\beta_1=\frac{3}{40},\quad \beta_2=0.0828,\quad \beta^*=\frac{9}{100},\sigma_{k1}=0.85,\quad \sigma_{k2}=1,$$

$$\sigma_{\omega 1}=0.5, and\ \sigma_{\omega 2}=0.856.$$

2.2.3 The Schnerr and Sauer Model (Cavitation Model)

Conforming to Bernoulli's principle, cavitation is the formation of vapor bubbles in the water near a rotating propeller blade in areas of low pressure. In order to calculate the pressure-induced phase transition of liquid into vapor and vice versa, the Schnerr-Sauer cavitation model [16] has been used in the study. In order to get the solution for a volume fraction, α, with an extra source term for evaporation and condensation, it needs to solve for a volume fraction, α, while adding an additional source term to the right-hand side of the Eq. (8).

$$\frac{\partial\alpha}{\partial t}+\nabla\cdot(\alpha\boldsymbol{U})=-\frac{\dot{m}}{\rho} \tag{8}$$

The continuity equation becomes,

$$\nabla\cdot\boldsymbol{U}=\left(\frac{1}{\rho_v}-\frac{1}{\rho_l}\right)\dot{m} \tag{9}$$

Here, $\dot{m}$ is the rate of change of mass, and ρ denotes the density of the liquid-vapor mixture. A formula for the mass transfer rate between the liquid and vapor is required in order to close the system of equations. The method of Sauer and Schnerr seems to be advantageous since it gives the position of a single bubble after the equation of motion is applied which is given in Eq. (10).

$$\dot{m}=\frac{\rho_1\rho_{\mathrm{v}}}{\rho}(1-\alpha)\alpha\frac{3}{R}\sqrt{\frac{\frac{2}{3}(p-p_{\mathrm{v}})}{\rho_{\mathrm{l}}}} \tag{10}$$

2.2.4 The Ffowcs Williams-Hawkings (FW-H) Acoustic Analogy

The FW-H is a solution to the Lighthill equation that has been created by Ffowcs Williams, John E., and David L. Hawkings [17]. FW-H formulation is utilized in the FVM to extract the total SPLs in the far field, which is then employed in the FVM. Following the suggestion made by Brentner and Farassat [18], the solution to the FW-H equation in the time domain was given by Brentner and Farassat where the pressure field is defined as follows:

$$P'(\vec{x},t)=P'_T(\vec{x},t)+P'_L(\vec{x},t) \tag{11}$$

$$4\pi P'_T(\overrightarrow{x},t)=\int_{f=0}\left[\frac{\rho_o\frac{\partial v_n}{\partial t}}{r(1-M_r)^2}\right]_{ret}dS+\int_{f=0}\left[\frac{\rho_o\frac{\partial v_n}{\partial t}\left(r\frac{\partial M_1}{\partial t}\widehat{r_i}+C_oM_r-C_oM^2\right)}{r^2(1-M_r)^3}\right]_{ret}dS \tag{12}$$

$$4\pi P_T'(\overrightarrow{x},t) = \frac{1}{C_0}\int_{f=0}\left[\frac{l_1\widehat{r_i}}{r(1-M_{r)}{}^2}\right]_{ret} dS + \int_{f=0}\left[\frac{l_r - l_iM_i}{r^2(1-M_{r)}{}^2}\right]_{ret} dS + \frac{1}{C_0}\int_{f=0}\left[\frac{\rho_0 v_n(r\frac{\partial M_1}{\partial t}\widehat{r_i} + C_oM_r - C_oM^2)}{r^2(1-M_{r)}{}^3}\right]_{ret} dS \qquad (13)$$

Here, P' is the total acoustic pressure, which is made up of P_T' and P_L' which denote the different degrees of acoustic pressure caused by thickness and loading in relation to the monopole and dipole sound sources, respectively. Blade rotation and unstable sheet cavitation on blades, for example, are classified as monopole sources, while the fluctuation pressure on the blade surface is classified as a dipole. Where (r = |x(t) y(t)|) denotes the distance between receiver and source, whereas x and t denote the location of the sound receiver on the time axis and the time at which the sound has been received. y and t are also specified as the location and time of the source, respectively. To begin, the flow around the marine propeller is measured in order to identify the causes of noise. When the RANS equations are solved, it is possible to extract the flow field of the propeller from the FVM. As integral surfaces, f = 0, the surfaces of the marine propeller blades will be chosen as integral surfaces for use in the simulation.

2.2.5 Structural Analysis Equations

The pressure load delivered to the proposed marine propellers will be calculated using the one-way FSI technique in a steady condition. The following finite element equation for static analysis [11].

$$Ku = F \qquad (14)$$

Here, K, u, and F are the stiffness matrix of the propeller, the displacement vector of the propeller node, and the imported pressure load applied on the propeller respectively.

The design will be safe if,

$$\sigma = \tfrac{1}{2}(\sigma_1 - \sigma_2) < \sigma_{\max}, \qquad (15)$$

where, σ and $\sigma_{\max}$ are main shear stress and maximum principle stress, respectively. The Von Mises stress is [19],

$$\bar{\sigma} = \tfrac{1}{\sqrt{2}}\sqrt{(\sigma_1-\sigma_2)^2 + (\sigma_2-\sigma_3)^2 + (\sigma_3-\sigma_4)^2}. \qquad (16)$$

The factor of safety is,

$$N_f = \tfrac{S}{\bar{\sigma}}, \qquad (17)$$

where, S and $\bar{\sigma}$ are the strength of the material and von mises stress respectively.

In the case of ANSYS static structural analysis, fixed support is applied to the direction of the axis of the shaft. Then the pressure loads from the ANSYS FLUENT are imported for each of the marine propellers. The analysis settings are the same for each static structural simulation described in Table 2.

After completing all setup in ANSYS static structural analysis, simulations are run for each rake angle of 4 types of both AU-outline GAWN series and B-series marine propellers by varying the materials such as Aluminium 6061 alloy, Nickel-Aluminium-Bronze (NAB), S2 glass, and carbon fiber reinforced plastic (CFRP).

Table 2 Details of analysis settings in static structural analysis

Step Controls	**Details**
Number of Steps	1
Current Step Number	1
Step End Time	1 s
Auto Time Stepping	Program Controlled
Solver Controls	
Solver Type	Program Controlled
Weak Springs	Off
Solver Pivot Checking	Program Controlled
Large Deflection	Off
Inertia Relief	Off

2.3 ANSYS Fluent Approach-CFD Analogy

The modeled Au-outline GAWN series and B-series marine propellers with the variation of rake angles of 0°, 5°, 10°, and 15° respectively (total 8 marine propellers) have been imported to ANSYS FLUENT. The computational domains-Fluid enclosure domain and Propeller domain are shown in Fig. 1. These domains are the same for each series of marine propellers of various rake angles. The inlet and outlet flow regions are also shown here.

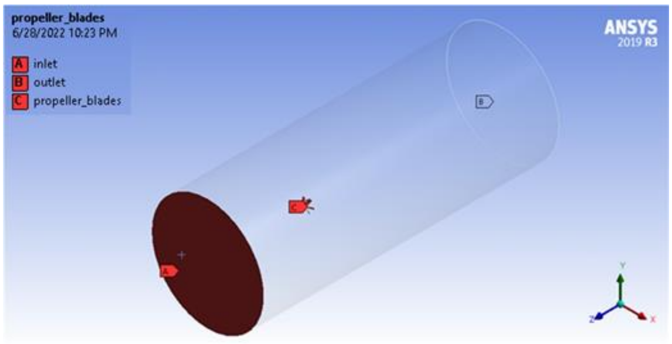

Fig. 1 General design of computational domains in FLUENT.

The inlet is placed at a distance of 2 m upstream from the propeller plane, and the outlet is placed at a distance of 4m downstream from the propeller plane. The domain dimensions considered are large enough to avoid external effects on the performance prediction of the propellers [20]. In the radial direction, the cylindrical domain has been kept at 1m in radius from the axis of the marine propeller hub. This has been the same for both AU-outline GAWN series and B-series marine propellers of rake angles of 0°, 5°, 10°, and 15° respectively. Before processing the solution in the Fluent solver, it is necessary to indicate fluid volumes and discretization of the infinite domain into a finite domain. Proper mesh generation is the key to accurate results. There are various types of mesh shapes-tetrahedral, quad-lateral, hexahedral, etc. In this study, tetrahedron mesh has been used for each series of modeled propellers of 4 types of rake angles. The mesh details are given in Table 3. A domain with a high grid number results in an accurate simulated result. However, the usage of a higher grid leads to high computational costs. It is observed that SPLs at 0° rake angle are approximately the same for the element number higher than 6,50,000. Thus, the element number of the domain was chosen according to Table 3.

Table 3 Mesh details of modeled propellers in ANSYS Fluent.

Propellers	**Rake Angles**	**Number of Nodes**	**Number of Elements**
AU-outline GAWN Series	0°	128175	685436
	5°	120682	646999
	10°	121496	649404
	15°	121496	649404
B-series	0°	122112	653717
	5°	123456	661193
	10°	124033	663485
	15°	125791	672804

After proper meshing of modeled marine propellers, the FLUENT solver tool was used to get the solutions and results. The boundary conditions that have been used in ANSYS FLUENT are tabulated in Table 4. The data on boundary conditions have been collected from Helal et al. [21] for cavitation conditions. The inlet condition is velocity controlled. Thus, Reynolds number influences at the input and the body of the wall is defined as no slip condition. The boundary conditions and solver details are given in Table 4.

Table 4 Boundary conditions and solver details [21].

Parameter	**Value**
Solver type	Pressure-based
Process	Transient
Velocity formulation	Absolute
Rotation speed of the propeller, n	3000 rpm (50 rps)
Inlet velocity	8 m/s
Advance ratio, J	0.71
cavitation number, σ	1.763
Outlet pressure	207072 Pa
Vapor pressure	2337 Pa

The Schnerr-Sauer cavitation model [16] has been used in ANSYS Fluent as a cavitation model. The liquid water and vapor water have been defined as phase-1 and phase-2 in the multiphase model, respectively. For phase interaction, one mass transfer mechanism has been used. For this, the Schnerr-Sauer cavitation model is activated and the vapor pressure is defined as 2337 Pa. For the viscous model, the SST k-ω turbulence model is used. The Ffowcs Williams-Hawkings equation, which can be derived from the basic conservation laws of mass and momentum written in terms of generalized functions, represents the theoretical basis for the analysis of sound generated by a body moving in a fluid. It is worth noting that the velocity v for marine propeller applications is very small in comparison to the sound speed C0, and thus the Mach number M is close to zero. Thus, the transient flow field is statistically constant while using the Ffowcs Williams-Hawkings (FWH) acoustic model. This criterion must be maintained to perform an ANSYS FLUENT transient solution. Thus, it is recommended to execute an ANSYS FLUENT transient solution until the transient flow field is "statistically constant" while using the Ffowcs Williams-Hawkings (FWH) acoustic model. This implies that the whole set of relevant flow variables, along with the unsteady flow field under consideration, has been completely formed to the point that its statistics are stable throughout time. It is possible to assess if this condition has been satisfied by keeping an eye on the key flow variables at specific locations across the domain. In this present study, four hydrophone acoustic receivers are defined in FW-H acoustic model in ANSYS Fluent. Acoustic receivers 1 and 2 are defined at 550 mm away horizontally from the modeled propeller during simulation. Similarly, hydrophones 3 and 4 were defined at 1000 mm (1 m) away horizontally from the propeller. After the end of the CFD solution in ANSYS FLUENT, the results data is collected and the pressure load is imported to static structural analysis.

2.4 ANSYS Static Structural Analysis Approach (One-Way Fluid-structure Interaction)

In the ANSYS structural analysis, the geometries of both AU-outline series and B-series marine propellers of 4 types of rake angles are imported for static structural simulation processes.

After the completion of all setup in ANSYS static structural analysis, simulations have been run for each rake angle of 4 types for both AU-outline GAWN series and B-series marine propellers by varying the materials such as Aluminum 6061 alloy, Nickel-Aluminum-Bronze (NAB), S2 glass, and carbon fiber reinforced plastic (CFRP). The properties of those materials are tabulated in Table 5 and Table 6.

Table 5 Properties of accommodated materials.

Parameters	**Materials**		
	Aluminum 6061 [21], [22]	Ni-Al-Br (NAB) [23]	CFRP [24]
Density (kg/m^3)	2360	2485	7590
Young's Modulus (GPa)	47.78	86	125
Shear Modulus (GPa)	26	35.5	47.3
Bulk Modulus (GPa)	68.9	49.4	115
Poisson's Ratio	0.33	0.21	0.32
Yield Strength (MPa)	276	310	-
Ultimate Strength (MPa)	310	621	3790

Table 6 Properties of S2 Glass [10].

Parameters	**S2 Glass**
Density (kg/m^3)	1800
Young's Modulus x direction (MPa)	22925
Young's Modulus y direction (MPa)	22925
Young's Modulus z direction (MPa)	12400
Poisson's Ratio xy	0.12
Poisson's Ratio yz	0.2
Poisson's Ratio zx	0.2
Shear Modulus xy (MPa)	4700
Shear Modulus xz (MPa)	4200
Shear Modulus yz (MPa)	4200
Tensile Ultimate Strength (MPa)	4890

3 Results and Discussion

3.1 Vapor Volume Fraction (Cavitation)

Since cavitation is the formation of vapor bubbles in the water near a rotating propeller blade in areas of low pressure (suction side), the vapor volume fraction contours and data are also collected after the end of the CFD simulations via ANSYS CFD Post-processing tool. The changes in cavitation values for different rake angles are shown in Fig. 2.

3.2 Acoustic Results (Cavitation Noise)

The data on noises caused by cavitation is collected in the form of sound pressure level (SPL) graphs at the end of the CFD simulation in the CFD post-process tool. The SPL data of simulated various rake angles of both AU-outline GAWN series and B-series marine propellers are shown in Fig. 3 and Fig. 4.

The graphs of cavitation noise (SPL) are calculated for 500 Hz frequencies in 4 different positions of acoustic receivers of simulated 0°, 5°, 10°, and 15° rake angles of AU-outline GAWN series and B-series marine propellers.

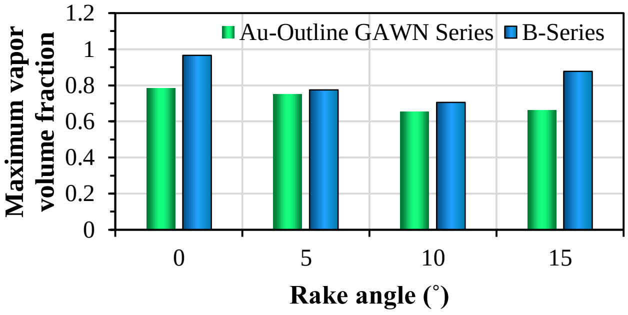

Fig. 2 Vapor fraction values for different rake angles

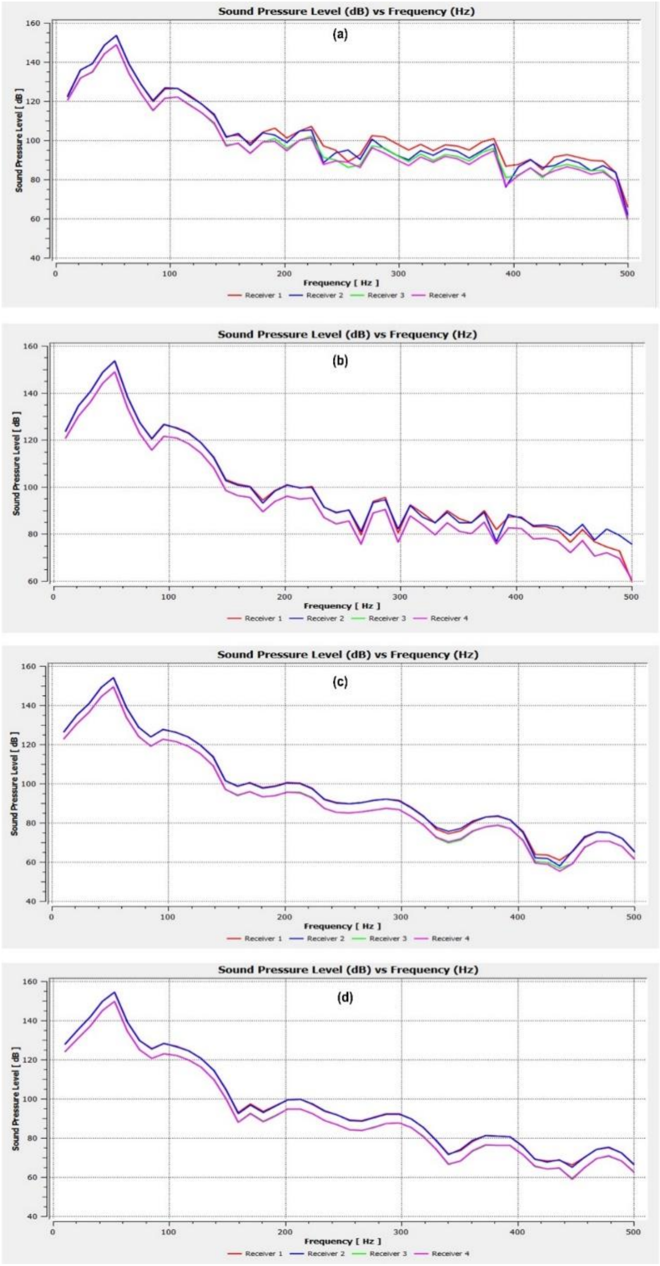

Fig. 3 Sound pressure level (dB) of (a) 0°, (b) 5°, (c) 10°, and (d) 15° rake angles of AU-outline GAWN series propellers

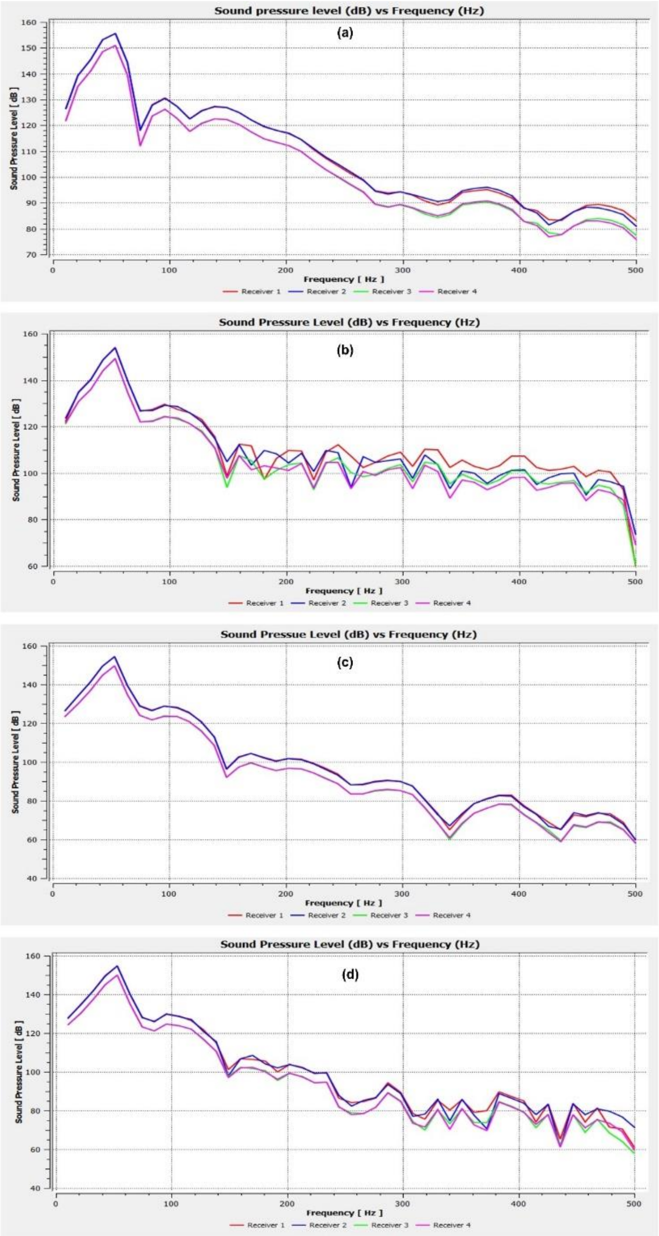

Fig. 4 Sound pressure level (dB) of (a) 0°, (b) 5°,(c) 10°, and (d) 15° rake angles of B-series propellers

The maximum sound pressure level (SPL) at 50 Hz frequency results are tabulated in Table 7 for both AU-outline GAWN series and B-series marine propellers.

Table 7 Maximum sound pressure level (dB) at 50 Hz frequency

Rake angles	**0°**	**5°**	**10°**	**15°**
AU-outline GAWN series	156.4 dB	154.2 dB	153.3 dB	157 dB
B-series	157.4 dB	155.9 dB	153.1 dB	156.6 dB

From the table, it can be observed that the lowest maximum sound pressure level (SPL) is found for 10° rake angle for both AU-outline GAWN and B-series marine propellers because the vapor volume fractions are the lowest at 10° rake angles of both AU-outline GAWN series and B-series marine propellers. The volume fraction values for the AU-outline GAWN series of marine propeller and B-series marine propeller are 0.653 and 0.705958 respectively at a 10° rake angle. The main sources of the sound pressure level are sheet cavitation since propeller geometry is one of the parameters that have effects on cavitation and its induced noise [25]. Thus, the rake angles of various propellers have different effects on cavitation noises. For this reason, changes in cavitation noises occur in different rake angles of propellers. For both AU-outline GAWN and B-series propellers, a 10° rake angle is found as the optimized rake angle with the lowest sound pressure level.

3.2.1 Static Structural Simulation Results

The pressure load generated from hydrodynamic characteristics influences the geometries of the blades and the hub of the propellers. In order to obtain the effects of materials, static structural simulation data is collected for 4 types of rake angles of both AU-outline GAWN series and B-series marine propellers for various materials such as Aluminum 6061 alloy, Nickel-Aluminum-Bronze (NAB), S2 glass, and carbon fiber reinforced plastic (CFRP). One-way FSI is used to obtain those data because only the effect of pressure load on the propellers and their materials has to be observed. The von-mises stresses for Aluminum 6061 alloy material are shown in Fig. 5 and Fig. 6 for AU-outline GAWN and B-series propellers, respectively.

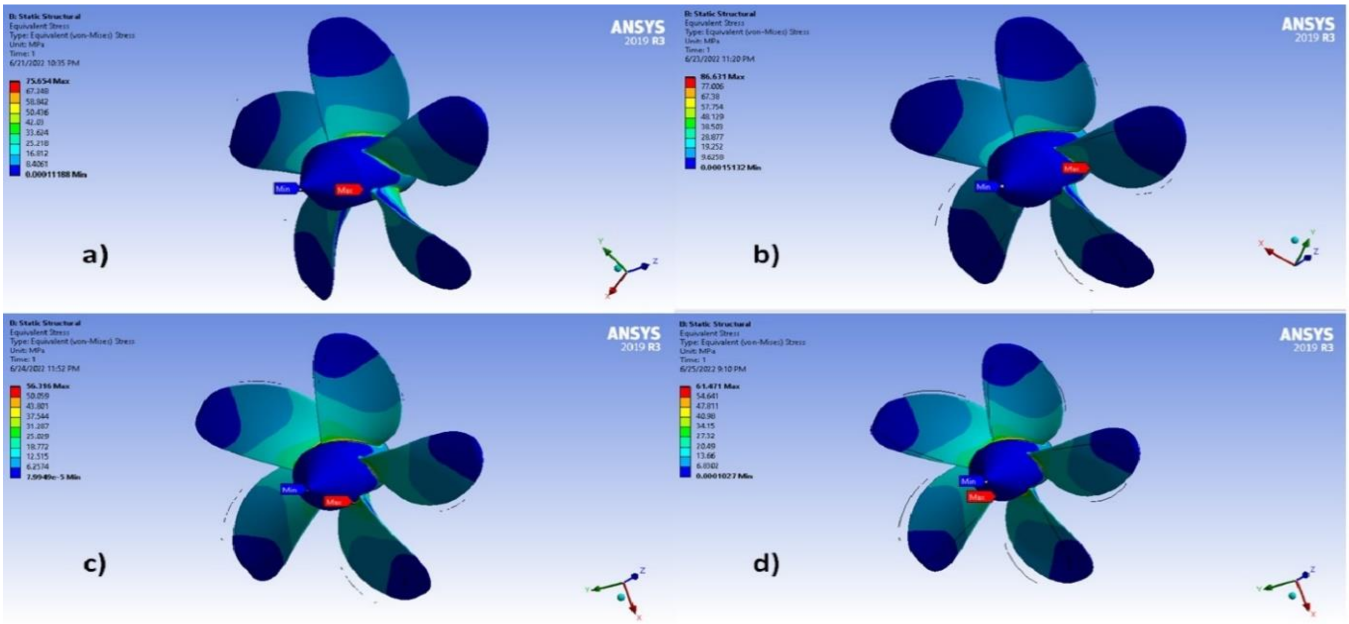

Fig. 5 Von-mises stresses of a) 0°, b) 5°, c) 10°, and d) 15° rake angles of AU-outline GAWN series propellers with Aluminum 6061 alloy material

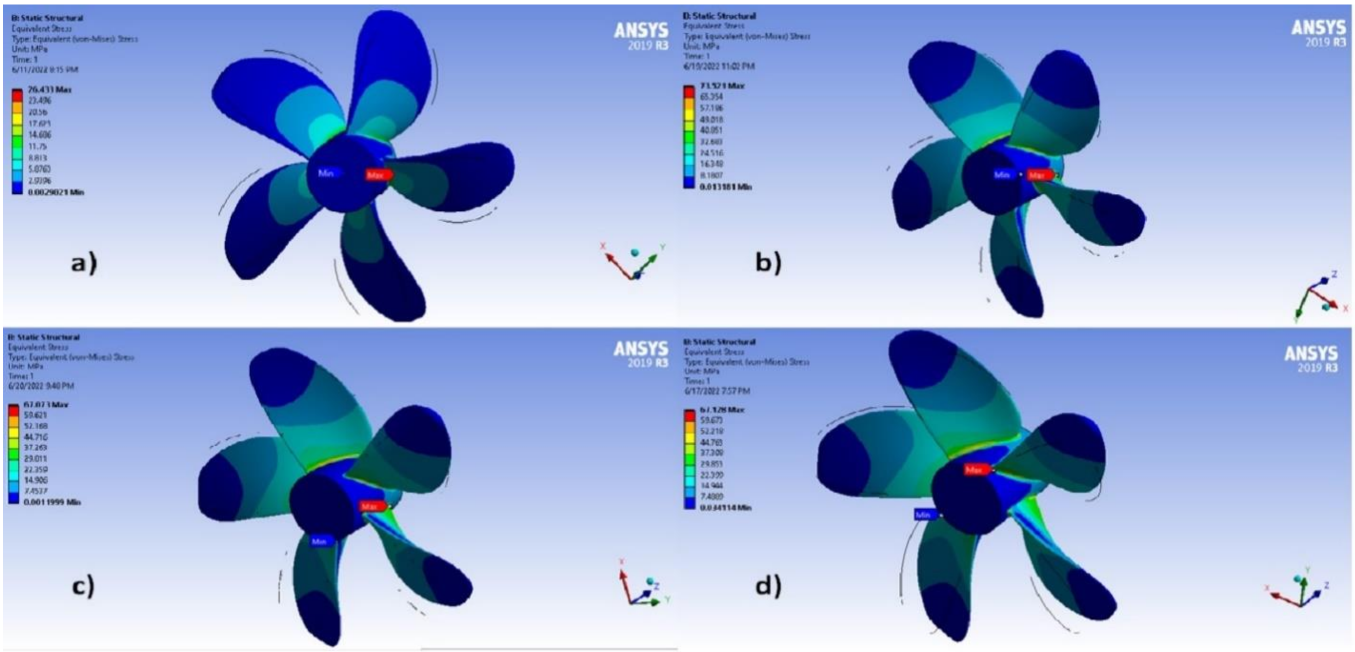

Fig. 6 Von-mises stresses of a) 0°, b) 5°, c) 10°, and d) 15° rake angles of B-series propellers with Aluminum 6061 alloy material

The effect of materials obtained for both AU-outline GAWN and B-series marine propellers of 0°, 5°, 10°, and 15° rake angles in static structural simulation. The best materials are chosen based on the lowest maximum Von-Mises stress results. Thus, the maximum von-mises stresses are demonstrated for AU-outline GAWN series and B-series marine propellers in Fig. 7 and Fig. 8, respectively. Aluminum 6061 alloy showed the lowest maximum von-mises stress among other materials. For example, Aluminum 6061 alloy material exhibited the lowest von-mises stress of 53.316 MPa at a 10° rake angle for AU-outline GAWN series marine propeller, while the Aluminum 6061 alloy material exhibited the lowest von-mises stress of 26.433 MPa at 0° rake angle for B-series marine propeller.

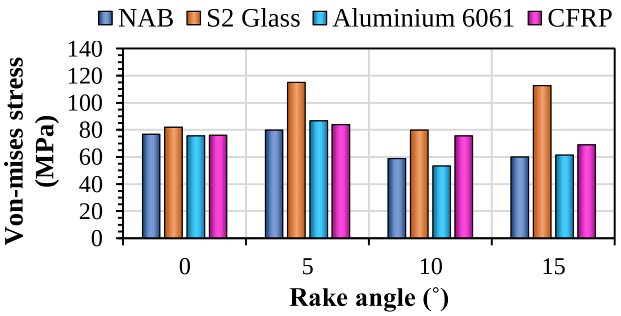

Fig. 7 Maximum Von-mises stresses for AU-outline GAWN series propellers

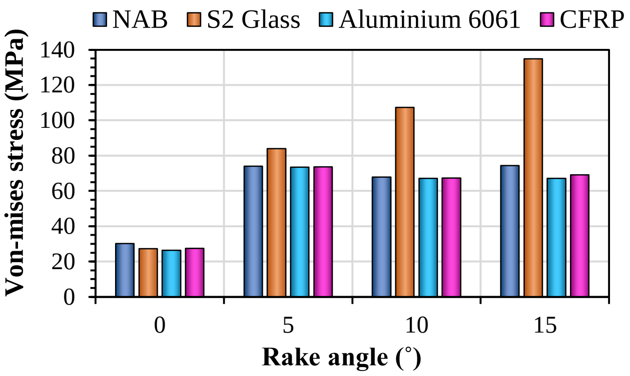

Fig. 8 Maximum Von-mises stresses for B-series propellers

The value of the factor of safety is demonstrated in Fig. 9 and Fig. 10, respectively. The maximum safety factor is observed for CFRP at a 10° rake angle for AU-outline GAWN series propeller. However, the maximum safety factor is observed for S2 glass at 0° rake angle for B-series marine propeller. The factor of safety for S2 glass is higher compared to other materials at low rake angles for both propellers, while the factor of safety for CFRP is higher compared to other materials at high rake angles for both propellers. Thus, S2 glass is the optimum material at a low rake angle for both propellers, while CFRP is the optimum material at a high rake angle for both propellers.

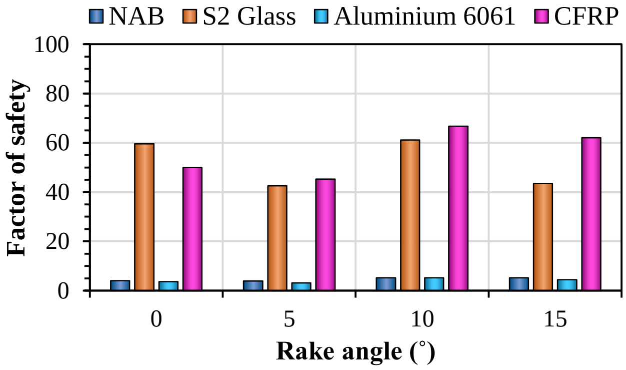

Fig. 9 Maximum factor of safety for Au-outline GAWN series propellers

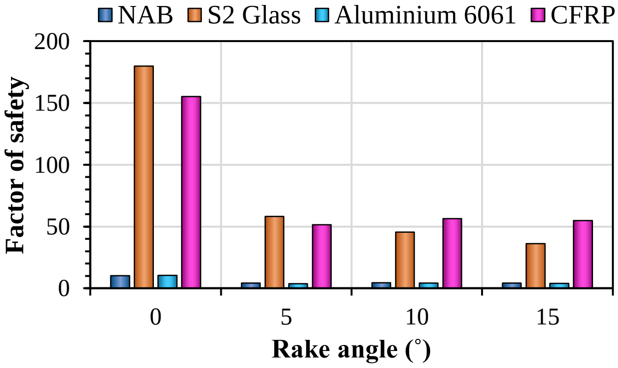

Fig. 10 Maximum factor of safety for B-series propellers

3.3 Comparison and Validation

The comparative results of sound pressure level (dB) up to 500 Hz frequency are illustrated in Fig. 11 with the Model II propeller in the article by Bagheri et al.[7] for a 0° rake angle. Fig. 11 shows that the variations with Bagheri et al. are 6.4 dB and 7.4 dB in maximum SPL for 0° rake angles of AU-outline GAWN and B-series propellers, respectively under cavitating conditions.

Another comparison of the simulated result of von-mises stress with Harish et al. [10] is illustrated in Fig. 12 for 0° rake angle for S2 glass and Aluminum 6061 alloy material in AU-outline GAWN and B-series propellers.

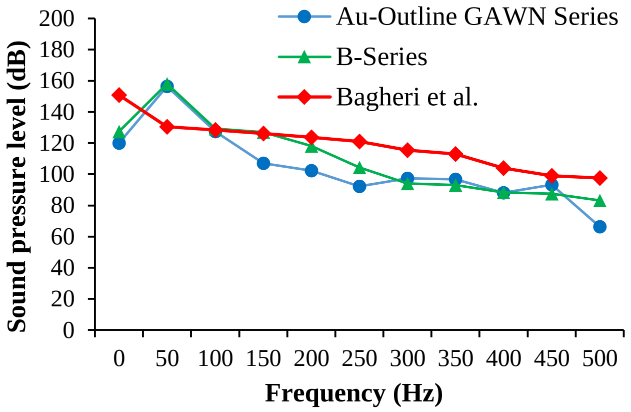

Fig. 11 Comparison of SPL with Bagheri et al. [7] for 0° rake angle.

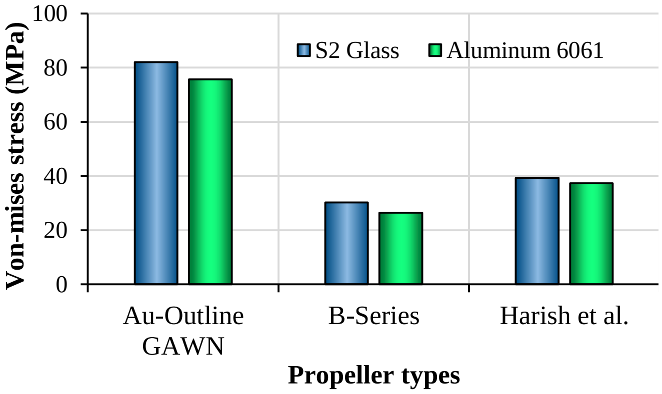

Fig. 12 Comparison of Von-mises stress with Harish et al. [10].

For S2 glass, the differences were 42.75 MPa and 9.069 MPa in AU-outline GAWN and B-series, respectively. For Aluminum 6061 material, the differences were 38.376 MPa and 10.845 MPa in AU-outline GAWN and B-series, respectively.

4 Conclusion

CFD analysis of both AU-outline GAWN series and B-series at 0°, 5°, 10°, and 15° rake angles reveals that the 10° rake angle for both series propellers is the most efficient because the cavitation and cavitation noise is the lowest in both AU-outline GAWN and B-series propellers at 10° rake angle. Moreover, upon conducting the static structural simulation in one-way fluid-structure interaction analysis, it is found that the von-mises stress values are lowest in the case of Aluminum 6061 alloy. However, S2 glass is the optimum material at low rake angles, while CFRP is the optimum material at high rake angles compared to all other potential materials for both AU-outline GAWN series and B-series propellers.

References

[1] Morgut, M. and Nobile, E., 2012. Influence of grid type and turbulence model on the numerical prediction of the flow around marine propellers working in uniform inflow. Ocean Engineering, 42, pp.26-34.

[2] Kerwin, J.E., 1986. Marine propellers. Annual Review of Fluid Mechanics, 18(1), pp.367-403.

[3] Abrahamsen, K., 2012, July 2012. The ship as an underwater noise source. In Proceedings of Meetings on Acoustics ECUA2012 (Vol. 17, No. 1, p. 070058). Acoustical Society of America.

[4] Wärtsilä Fixed Pitch Propellers. Available at https://www.wartsila.com/marine/products/propulsors-and-gears/propellers/wartsila-fixed-pitch-propellers. (Accessed 18 January, 2023.)

[5] Bertschneider, H., Bosschers, J., Choi, G.H., Ciappi, E., Farabee, T., Kawakita, C. and Tang, D., 2014. Specialist committee on hydrodynamic noise. Final report and recommendations to the 27th ITTC. Copenhagen, Sweden, 45.

[6] Lafeber, F.H., Bosschers, J. and van Wijngaarden, E., 2015, May. Computational and experimental prediction of propeller cavitation noise. In OCEANS 2015-Genova (pp. 1-9). IEEE.

[7] Bagheri, M.R., Seif, M.S., Mehdigholi, H. and Yaakob, O., 2017. Analysis of noise behaviour for marine propellers under cavitating and non-cavitating conditions. Ships and Offshore Structures, 12(1), pp.1-8.

[8] Usta, O., Aktas, B., Maasch, M., Turan, O., Atlar, M. and Korkut, E., 2017. A study on the numerical prediction of cavitation erosion for propellers. In Proceedings of the Fifth International Symposium on Marine Propulsors - SMP'17 12 - 15 June 2017, Espoo, Finland.

[9] Yamatogi, T., Murayama, H., Uzawa, K., Kageyama, K. and Watanabe, N., 2009, July. Study on cavitation erosion of composite materials for marine propeller. In 17th International Conference on Composite Materials Edinburgh, Scotland.

[10] Harish, B., Prasad, K.S. and Rao, G.U.M., 2015. Static Analysis of 4-Blade Marine Propeller. Journal of Aerospace Engineering & Technology, 5(2), pp.8-21.

[11] Yu, K., Yan, P. and Hu, J., 2020. Numerical analysis of blade stress of marine propellers. Journal of Marine Science and Application, 19, pp.436-443.

[12] Ghassemi, H., Gorji, M. and Mohammadi, J., 2018. Effect of tip rake angle on the hydrodynamic characteristics and sound pressure level around the marine propeller. Ships and Offshore Structures, 13(7), pp.759-768.

[13] Menter, F.R., 1994. Two-equation eddy-viscosity turbulence models for engineering applications. AIAA Journal, 32(8), pp.1598-1605.

[14] Wilcox, D.C., 1988. Reassessment of the scale-determining equation for advanced turbulence models. AIAA Journal, 26(11), pp.1299-1310.

[15] Hassan, T., Islam, M.T., Rahman, M.M., Ali, A.R.I. and Al Ziyan, A., 2022. Evaluation of different turbulence models at low reynolds number for the flow over symmetric and cambered airfoils. Journal of Engineering Advancements, 3(01), pp.12-22.

[16] Schnerr, G.H. and Sauer, J., 2001, May. Physical and numerical modeling of unsteady cavitation dynamics. In Fourth international conference on multiphase flow (Vol. 1). New Orleans, LO, USA: ICMF New Orleans.

[17] Ffowcs Williams, J.E. and Hawkings, D.L., 1969. Sound generation by turbulence and surfaces in arbitrary motion. Philosophical Transactions of the Royal Society of London. Series A, Mathematical and Physical Sciences, 264(1151), pp.321-342.

[18] Brentner, K.S. and Farassat, F., 2003. Modeling aerodynamically generated sound of helicopter rotors. Progress in Aerospace Sciences, 39(2-3), pp.83-120.

[19] Budynas, Richard Gordon and Nisbett JK and others, 2011. Shigley’s mechanical engineering design. McGraw-Hill, New York.

[20] Hayati, A.N., Hashemi, S.M. and Shams, M., 2012. A study on the effect of the rake angle on the performance of marine propellers. Proceedings of the Institution of Mechanical Engineers, Part C: Journal of Mechanical Engineering Science, 226(4), pp.940-955.

[21] Helal, M.M., Ahmed, T.M., Banawan, A.A. and Kotb, M.A., 2018. Numerical prediction of sheet cavitation on marine propellers using CFD simulation with transition-sensitive turbulence model. Alexandria Engineering Journal, 57(4), pp.3805-3815.

[22] Seli, H., Awang, M., Ismail, A.I.M., Rachman, E. and Ahmad, Z.A., 2013. Evaluation of properties and FEM model of the friction welded mild steel-Al6061-alumina. Materials Research, 16, pp.453-467.

[23] ASM Material Data Sheet, Available at: http://asm.matweb.com/search/SpecificMaterial.asp?bassnum=MA2024T4. (Accessed on 12th November 2022).

[24] Uddin, M.M., Hossen, M.P., Jahan, M.M. and Islam, M.I., 2021, February. Structural analysis of composite propeller of ship using FEM. In AIP Conference Proceedings (Vol. 2324, No. 1, p. 030001). AIP Publishing LLC.

[25] Sharma, S.D., Mani, K. and Arakeri, V.H., 1990. Cavitation noise studies on marine propellers. Journal of Sound and Vibration, 138(2), pp.255-283.

This page is left intentionally blank

Journal of Engineering Advancements (JEA)

DOI: https://doi.org/10.38032/jea

Indexed by:

Google Scholar Crossref

Scilit

Volume 04 Issue 01

DOI: https://doi.org/10.38032/jea.2023.01

Published by: SciEn Publishing Group

Website: www.scienpg.com